



5-2000

Volumetric reconstruction in the microCAT tomography system

Joshua Edward Cates

Follow this and additional works at: https://trace.tennessee.edu/utk_gradthes

Recommended Citation

Cates, Joshua Edward, "Volumetric reconstruction in the microCAT tomography system. " Master's Thesis, University of Tennessee, 2000.
https://trace.tennessee.edu/utk_gradthes/9294

This Thesis is brought to you for free and open access by the Graduate School at TRACE: Tennessee Research and Creative Exchange. It has been accepted for inclusion in Masters Theses by an authorized administrator of TRACE: Tennessee Research and Creative Exchange. For more information, please contact trace@utk.edu.

To the Graduate Council:

I am submitting herewith a thesis written by Joshua Edward Cates entitled "Volumetric reconstruction in the microCAT tomography system." I have examined the final electronic copy of this thesis for form and content and recommend that it be accepted in partial fulfillment of the requirements for the degree of Master of Science, with a major in Computer Science.

Jens Gregor, Major Professor

We have read this thesis and recommend its acceptance:

Michael G. Showasm

Accepted for the Council:

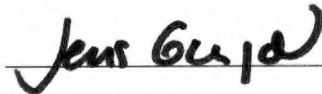
Carolyn R. Hodges

Vice Provost and Dean of the Graduate School

(Original signatures are on file with official student records.)

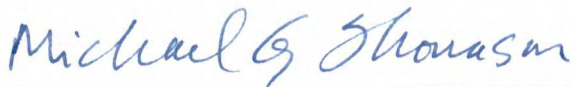
To the Graduate Council:

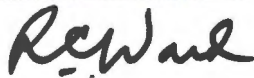
I am submitting herewith a thesis written by Joshua Edward Cates entitled "Volumetric Reconstruction in the MicroCAT Tomography System". I have examined the final copy of this thesis for form and content and recommend that it be accepted in partial fulfillment of the requirements for the degree of Master of Science, with a major in Computer Science.



Jens Gregor, Major Professor

We have read this thesis
and recommend its acceptance:





Accepted for the Council:



Associate Vice Chancellor
and Dean of the Graduate School

Volumetric Reconstruction in the MicroCAT Tomography System

A Thesis

Presented for the

Master of Science

Degree

The University of Tennessee, Knoxville

Joshua Cates

May 2000

Acknowledgments

I would first like to thank Dr. Jens Gregor for the many invaluable consultations and encouragements throughout the course of this research, and for the introduction to the fascinating world of image processing. I would also like to thank Shaun Gleason of the Oak Ridge National Laboratory for his support in providing essential data and an intimate knowledge of the MicroCAT system. Dr. Sam Jordan of the University of Tennessee Mathematics Department has my thanks for the solution to a particularly nasty integral. And lastly, I want to acknowledge my wonderful family for giving me an enthusiasm for learning that has sustained me my entire academic career.

Abstract

A new system for x-ray cone-beam micro-tomography has been developed to screen mice for internal phenotypic abnormalities at the Oak Ridge National Laboratory Mammalian Genetics Facility. Currently this system uses an image reconstruction algorithm that is based on two-dimensional (fan-beam) reconstruction techniques. The disparity between the actual scanner geometry and that assumed for reconstruction purposes introduces artifacts into the reconstruction volume that become increasingly worse the further their axial distance from the midplane. In order to reconcile this disparity and reduce axial distortion artifacts, a volumetric reconstruction algorithm based on cone-beam geometry was implemented. The volumetric algorithm is derived and its heuristic implementation is explained within the constraints of the system, which limit the arclength of the scanning trajectory. Reconstructions using the volumetric algorithm are analyzed and compared to reconstructions from the current method. We show that our implementation produces images of equivalent quality in the midplane, and a marked decrease in axial distortion elsewhere. Volume reconstruction times are shown to be comparable to those currently achieved. The theoretical foundations are given for future work to optimize the implementation through parallelization and by overcoming the data sufficiency problem.

Contents

1	Introduction	1
2	The Feldkamp cone-beam reconstruction algorithm	10
2.1	Mathematical foundations of tomography	11
2.2	Fan-beam reconstruction formula	15
2.3	Cone-beam reconstruction formula	17
2.4	Data completeness and the generalized Feldkamp formula	24
3	Implementation issues	27
3.1	Discretized Feldkamp	27
3.2	Computer implementation	32
3.3	Compensation techniques for short-scans	36
3.4	Further enhancements	47
4	Experimental results	50
5	Conclusions	66

A

77

Vita

81

List of Tables

4.1	Reconstruction times from Fig 4.4 rounded to nearest minute. .	59
-----	--	----

List of Figures

1.1	Scanning geometry of the MicroCAT system	6
1.2	Top view of MicroCAT scanning geometry, showing the path of fan-beams through the object to the detector array	6
2.1	Parallel-beam geometry	12
2.2	Fan beam geometry	16
2.3	Cone-beam geometry Note that in the derivation, $D = 0$	19
3.1	A matrix of projection data	30
3.2	Illustration of Feldkamp filtered backprojection algorithm	32
3.3	Symmetry of and relationship between the minimally complete data sets of the two dimensional Radon transforms of fan-beam acquired data g and parallel-beam data p	39
3.4	Symmetry of the Radon transform g in the range $0 \leq \Phi \leq 2\pi + 2\delta$	42
3.5	Weighting imbalance in the reconstructed image from backprojection over a minimally complete set of angles	45

4.1	A comparison of short-scan compensation techniques	52
4.2	Comparison of mouse reconstruction using (a) Parker weighting and (b) missing data recreation technique	54
4.3	Comparison of filtering techniques	56
4.4	Comparison of the effects of downsampling and bi-linear interpolation on image quality.	58
4.5	Axial distortion comparison of the fan-beam algorithm with the Feldkamp algorithm.	61
4.6	Relative distances along detector array of slices shown in Fig. 4.5.	62

Chapter 1

Introduction

A new system for x-ray computed tomography is under development at the Oak Ridge National Laboratory. This system is designed to function for a specific research application, but the current algorithmic implementation of that system needs improvement. This thesis addresses that need. This section will introduce the problem and propose a solution.

The Mammalian Genetics Research Facility at the Oak Ridge National Laboratory (ORNL) conducts research into the genetic effects of mammalian exposure to radiation and to other mutagenic sources. The facility houses over 70,000 mice comprised of around 400 mutant lines. Mutagenic experiments are conducted on the mice and the phenotypic manifestations of induced genetic abnormalities are studied. Studies currently require a physical and behavioral screening process that is slow and costly. Many phenotypic abnormalities are internal and cannot be found without killing the mouse.

To reduce the time and cost of internal abnormality screening, a Laboratory-Directed Research and Development program was started at ORNL. Under the scope of this program, a new x-ray computed tomography system was developed specifically for the phenotypic screening of the mice. This system is called the MicroCAT [9, 3]

The MicroCAT instrument acquires images on a CCD/phosphor screen detector as projections through an object from a point x-ray source. The detector is constructed of a 1024 x 1024 pixel CCD array bonded to a phosphor screen with a 2:1 fiber optic taper sandwiched in-between. The phosphor screen provides sensitivity to x-ray energies. The fiber optic taper doubles the imaging area and pixel size. The effective imaging area is approximately 50 x 50 mm². The effective pixel size is approximately 50 x 50 μm². The source and the detector move in tandem in a circular orbit around the object.

Data acquisition and the x-ray source trajectory are controlled by software running on a Windows NT workstation. A single 1024 x 1024 pixel projection is acquired in 2-3 seconds. A typical low-resolution data set consisting of 195 projections over 3.4 radians at regular angular intervals can be acquired in about 7 minutes. Higher resolution scans of up to 500 projections are acquired in 15-25 minutes.

Currently, image reconstruction from MicroCAT-acquired data is done using two-dimensional reconstruction techniques. In order to use two-dimensional algorithms, an (incorrect) assumption is made, namely, that projection data is acquired as fan-beam projections. In fan-beam tomography, a collimator is placed in front of the x-ray source so that only a thin plane of x-rays passes through the object. Rays diverging from

the source and passing through the collimator form a fan-shaped beam. This beam produces a one-dimensional projection. A set of projections at angular intervals around the object (a sinogram) provide data for a single slice of the reconstructed volume. A set of slices at intervals along the third dimension of the object can be stacked together to form a three-dimensional approximation of the object.

Fan-beam reconstruction is a well understood and straightforward approach to tomographic reconstruction [11]. A common method for reconstructing fan-beam slices is filtered backprojection. Filtered backprojection is the iterative process of summing weighted and filtered values from the sinogram into their appropriate locations in the reconstructed image. Each coordinate in the reconstruction matrix maps to some interpolated location in every projection array in the sinogram. This mapping is the backprojection step. The filtering step removes blurring that results from the backprojection. The mathematics behind filtered backprojection are described in the next section.

The current MicroCAT reconstruction technique performs the extra step of rebinning the fan-beam data so that it appears to have originated from a parallel-beam geometry. The parallel-beam scanner geometry, though often impractical to implement in reality, has several algorithmic advantages over a fan-beam geometry. The biggest advantage is that only π radians worth of angular projections are needed in the filtered backprojection algorithm. True fan-beam reconstruction requires a full 2π radians of projections¹. By

¹Heuristic methods have been developed to enable fan-beam reconstruction from $p\pi$ radians plus one cone-angle.

rebinning the data into this geometry, the MicroCAT system benefits from parallel-beam reconstruction advantages

Major advantages of the current reconstruction technique are its ease of implementation and fast reconstruction times for individual slices. The process of three-dimensional (volumetric) reconstruction by stacking two-dimensional reconstructions is a standard approach to tomographic imaging of volumes. The implementation of the reconstruction algorithm is therefore well understood. Scan-times and hardware costs are reduced by the additional step of rebinning to parallel data since source and detector only need to travel around half of the object's circumference

The major problem with the current reconstruction technique is that it is based on the wrong scanner geometry. Computed tomography systems using fan-beam geometries are known as second-generation scanners [5]. The MicroCAT system, however, is not a second-generation scanner. In the MicroCAT system, two-dimensional projection data is acquired from an uncollimated point source. Removing the collimator from the point source results in a cone-shaped beam. This *cone-beam* is centered at the middle of the object and moves along a circular trajectory around the object. The source does not need to be translated along the third-dimension as in fan-beam because the third-dimension is captured by the spread of the cone. Thus the MicroCAT system acquires data like a third-generation scanner, which are designed for volumetric (three-dimensional), as opposed to slice-by-slice (two-dimensional), tomography. The MicroCAT system differs from a true third-generation scanner because it is currently

only able to complete scans of about 3.85 radians. This limitation hinders its ability to perform volumetric reconstructions, which are usually based on full-circle trajectories.

Fig. 1.1 illustrates the actual scanning geometry of the MicroCAT system. The subset of rays from the cone-beam incident on the square detector array can be thought of as a *fan* of fan-beams. Each fan defines a plane at a particular inclination or declination from the midplane. The *midplane* of the system is the plane perpendicular to the axis of rotation that contains a ray from the source to a point on the axis of rotation (the center of rotation). The specimen to be scanned sits on a bed within the cylinder described by the detector's rotation.

In the current reconstruction technique, distortion occurs in the backprojection step. Fig. 1.2 shows a top view of the two scanner geometries. The upper configuration represents the assumed geometry of the current reconstruction method and the bottom configuration is the actual geometry. From Fig. 1.2 we can see that, with the exception of the center column, a ray-sum² collected on a detector array coordinate has resulted from attenuation through an entirely different set of points in the object than is assumed. Therefore, when this ray-sum is backprojected according to the assumed geometry, it is backprojected into the wrong points. The effect is minimized by a narrow cone-angle, since at narrow angles the difference between the real and assumed geometries is minimized. In fact, as the source-to-detector distance goes to infinity, the cone angle becomes infinitely small, and the cone-beam geometry degenerates into the parallel

²Line integral along the path of a ray

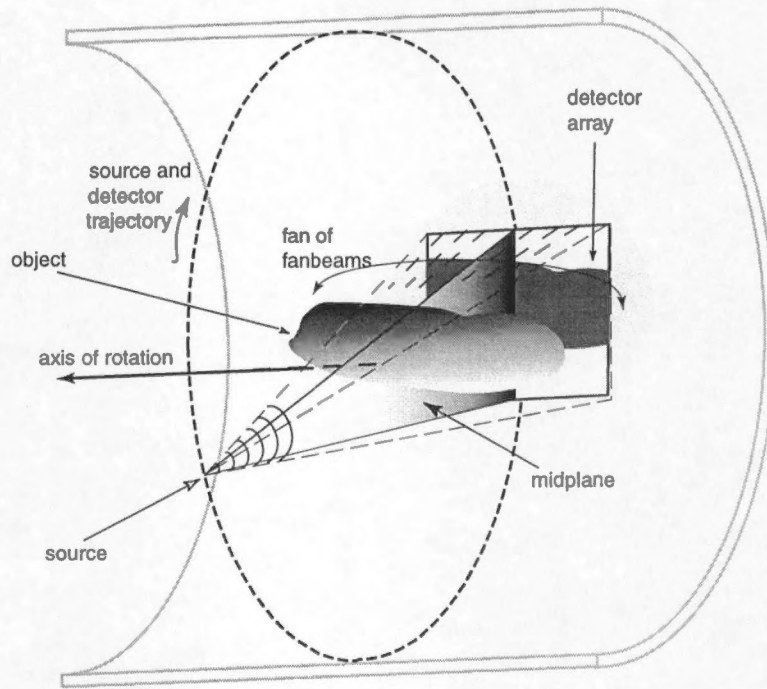


Figure 1.1: Scanning geometry of the MicroCAT system.

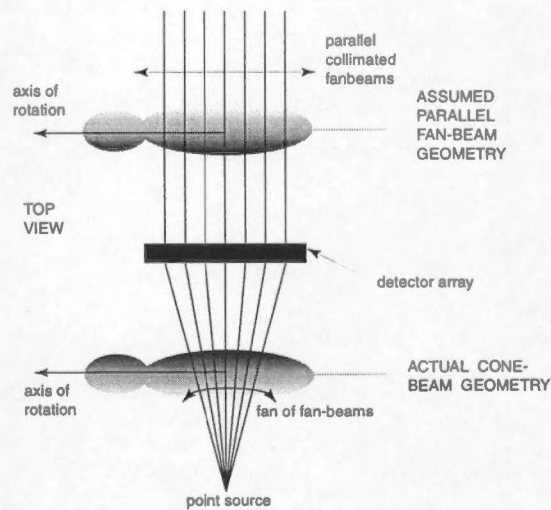


Figure 1.2: Top view of MicroCAT scanning geometry, showing the path of fan-beams through the object to the detector array.

beam geometry.

The cone angle of the MicroCAT system is 11.358 degrees and thus, in fact, relatively narrow. Also, in the midplane, the cone-beam geometry degenerates exactly to the fan-beam geometry. Slices near the center of its reconstructed volumes are therefore not greatly affected by an assumption of a fan-beam geometry. The current technique is therefore acceptable for many applications. But, in reality, only the center slice is correct. As one moves out from the center, slices show progressively more distortion.

Because of the distortion that results using the current technique, there is a need in the MicroCAT system for a new, volumetric reconstruction algorithm. An algorithm based on a three-dimensional geometry should eliminate much of the structural distortion towards the ends of the object. Ideally, such an algorithm should not significantly increase reconstruction time and should operate within the existing hardware constraints of the system.

There are a number of approaches to cone-beam tomographic reconstruction. The most common technique is to perform an inversion of the mapping from the three-dimensional space of the object to the two-dimensional projection space. This amounts to inverting the Radon transform of the object's density function. The inverted Radon transform reconstruction technique results in a *filtered backprojection* of the data. The Radon transform and filtered backprojection are discussed more fully in the next section. There have been a number of algorithms developed using this and other approaches. Good reviews of these algorithms can be found in [13, 1, 10, 12]

The choice of a cone-beam algorithm for the MicroCAT system is constrained somewhat by the design of the MicroCAT hardware. Data is acquired in a circular trajectory. Of the existing circular-trajectory algorithms for cone-beam reconstruction, that of Feldkamp et al. [2] has become a standard. The so called Feldkamp algorithm is based on filtered backprojection, which is computationally more efficient than most other cone-beam methods [10]. The Feldkamp algorithm is widely used in practice, and is considered to be among the most efficient of the filtered backprojection techniques [13].

Aside from its computational efficiency, another reason for choosing the Feldkamp algorithm, is that it is easily extended to a more general family of cone-beam algorithms developed by Wang et al. [16]. Wang extends the Feldkamp algorithm from circular to arbitrary source trajectories under certain conditions, which can be used to acquire a more complete set of views of the object than a circular trajectory will allow. The dimensions of the MicroCAT system are such that to image the full length of a mouse requires up to three separate reconstructions, which is not an ideal situation because of artifacts that result in regions of overlap between the reconstructions. Ideally, imaging an entire mouse specimen should be done using a helical orbit [1], which completely samples the object in a single scan. The Feldkamp algorithm can be easily extended to accommodate this type of orbit.

The Feldkamp algorithm is not exact. Artifacts result from the circular orbit (hence incomplete data) and from assumptions made in the derivation. The relative ease of

implementation and computational efficiency justify these artifacts for the MicroCAT application, especially since the present reconstruction method suffers from far worse approximations.

A final reason for choosing the Feldkamp algorithm for the MicroCAT system, is the ease with which it can be parallelized to reduce reconstruction times. Reconstruction speed is very important to the goal of reducing mouse screening times and cost. It will be apparent from the discussion of the implementation of the algorithm, that the convolution-backprojection operations of Feldkamp are readily parallelized to speed up the application in a linear fashion.

With the above rationale in mind, the logical choice for the MicroCAT system is the Feldkamp algorithm. This work documents the theory and implementation of this volumetric reconstruction technique given the system's current configuration and limitations. It also discusses possible improvements to the system and the theoretical basis behind those improvements. Experimental evidence is given to support theoretical claims, and conclusions are drawn about the effectiveness of the implementation.

This section has discussed the origins of the problem addressed in this thesis. A possible solution to that problem was proposed and evidence was offered as to the plausibility of the solution. The next section will outline the heuristic development of the Feldkamp algorithm and its underlying mathematical foundations.

Chapter 2

The Feldkamp cone-beam reconstruction algorithm

This section introduces some of the mathematical foundations of cone-beam tomography and the Feldkamp reconstruction algorithm. First, the Radon transform, filtered backprojection, and the projection theorem are defined. These three concepts are necessary for the development of the two-dimensional parallel-beam reconstruction case. Then, starting with the parallel-beam case, the necessary geometrical modifications are made to expand the parallel beam algorithm first into a fan-beam geometry, and then into fan-beam's three-dimensional analogue. This three-dimensional analogue is the Feldkamp algorithm. This section also introduces the data completeness condition and talks about how the Feldkamp algorithm can be extended to satisfy it.

2.1 Mathematical foundations of tomography

Fundamental to the mathematics of tomography, and necessary for the understanding of the development of the Feldkamp algorithm, is the concept of the Radon transform. Let f represent the density function of the scanned object as in Fig. 2.1, which shows the parallel-beam geometry. Projection data is the set of line integrals along the path of parallel rays emanating from the x-ray source and passing through f . This set of line integrals for all projection angles θ is known as the Radon transform of f . We represent the Radon transform operator, or *projection operator*, as \mathcal{R} . If δ is the delta function, then for f in polar coordinates where $x = r \cos \phi$, $y = r \sin \phi$ and $r = \sqrt{x^2 + y^2}$, the two-dimensional Radon transform in the parallel-beam geometry is,

$$\mathcal{R}f = g(l, \theta) = \int_{-\infty}^{\infty} \int_0^{2\pi} r f(r, \phi) \delta(r \cos(\theta - \phi) - l) d\phi dr \quad (2.1)$$

where $g(l, \theta)$ represents the value of the line integral along a ray through f at a distance l and angle θ .

The Radon transform allows us to define the next important concept, filtered back-projection. Since scanning an object amounts to taking the Radon transform of its density function, it seems logical that to reconstruct the density function, we need to somehow invert the Radon transform. *Backprojection* is an operation that maps a function in the Radon transform domain into the spatial domain of f and it is therefore a logical place to start in the development of such an inverse. In backprojection, each

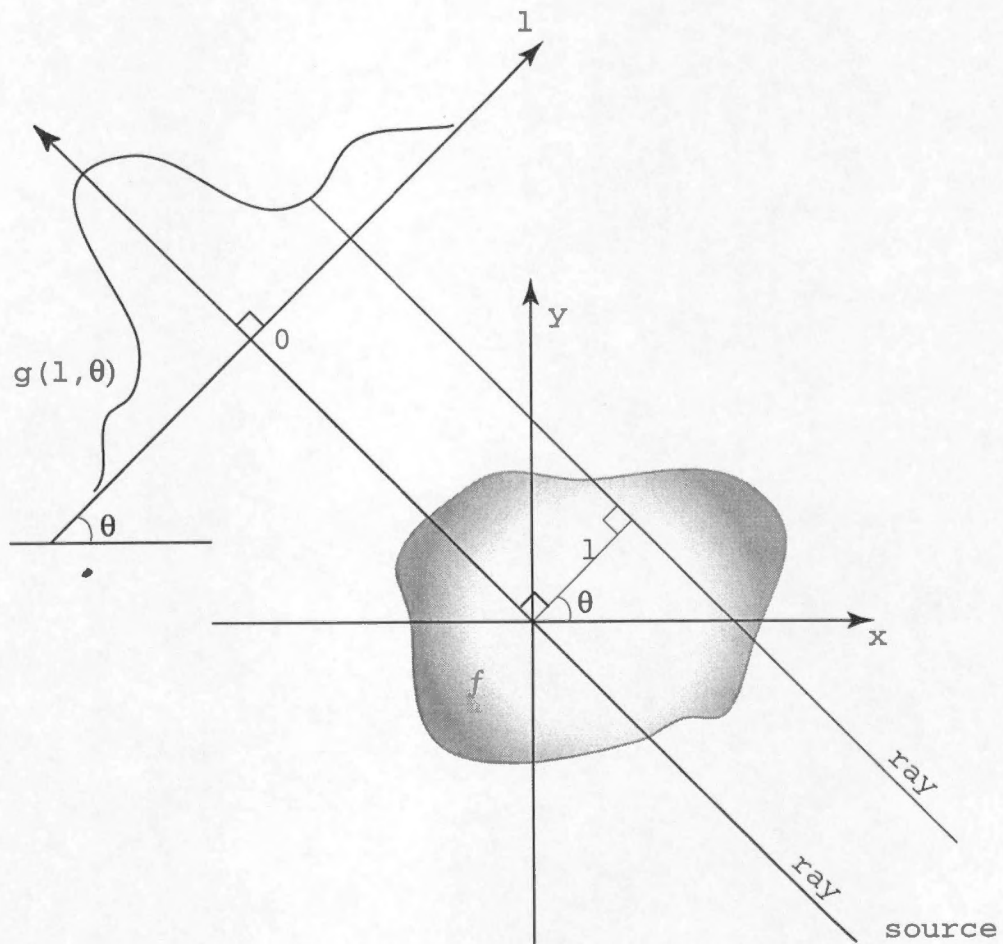


Figure 2.1: Parallel-beam geometry

point (l, θ) in the Radon transform is mapped back to a line in the spatial domain. This means that a single point in the spatial domain corresponds to multiple points in the Radon transform (one for each θ). Values mapping from different θ 's in the Radon transform to the same point in the spatial domain are summed.

But the backprojection operator \mathcal{B} is not the inverse of the projection operator. In fact, it can be shown that backprojecting the Radon transform of f ,

$$\tilde{f}(\vec{r}) = \mathcal{B}\mathcal{R}f(\vec{r}) \quad (2.2)$$

is an approximation of f blurred by a point-spread function $1/||\vec{r}'||$ [6], where \vec{r}' is of arbitrary dimension. To remove this blurring, we can introduce a filtering operation \mathcal{H} before backprojecting and achieve the final form of the filtered backprojection equation,

$$f(\vec{r}) = \mathcal{B}\mathcal{H}\mathcal{R}f(\vec{r}) \quad (2.3)$$

We now introduce the *projection theorem*. The projection theorem defines a relationship between the two-dimensional Fourier transform F of function f and the one-dimensional Fourier transform of its Radon transform $g(l, \theta)$ with respect to l . Specifically, if \mathcal{F} is the Fourier transform operator and $\mathcal{F}\{g\} = q(\omega, \theta)$, then the projection theorem states that the central slice $F(\omega \cos \theta, \omega \sin \theta)$ of F is equivalent to $q(\omega, \theta)$. The proof of this theorem can be shown by substituting Eqn 2.1 into the definition of the Fourier transform of g [6]

Using the projection theorem, we can write the inverse of the Radon transform of f as [6, 4],

$$f(r, \phi) = \frac{1}{4\pi^2} \int_0^{2\pi} \int_{-\infty}^{\infty} \frac{1}{r \cos(\theta - \phi) - l} \frac{\partial}{\partial l} g(l, \theta) dl d\theta \quad (2.4)$$

Eqn. 2.4 contains a singular integral. Note that $g(l, \theta) = \mathcal{F}^{-1}\{q(\omega, \theta)\}$ or,

$$g(l, \theta) = \frac{1}{2\pi} \int_{-\infty}^{\infty} q(\omega, \theta) \exp(i\omega l) d\omega \quad (2.5)$$

Substituting Eqn. 2.5 into Eqn. 2.4 and performing principal-value integration on the inner integral removes the singular integral and the partial, reducing to the form (see Appendix),

$$f(r, \phi) = \frac{1}{8\pi^2} \int_0^{2\pi} \int_{-\infty}^{\infty} |\omega| q(\omega, \theta) \exp[i\omega r \cos(\theta - \phi)] d\omega d\theta \quad (2.6)$$

By inverting the Fourier transform q we arrive at the final Radon inversion equation for the parallel-beam geometry [2],

$$f(r, \phi) = \int_0^{2\pi} \tilde{P}_\theta(l(r, \phi)) d\theta \quad (2.7)$$

$$\tilde{P}_\theta(l(r, \phi)) = \text{Re} \frac{1}{4\pi^2} \int_{-\infty}^{\infty} \int_0^{\infty} \omega P_\theta(l(r, \phi)) \exp[i\omega (r \cos(\theta - \phi) - l)] d\omega dl \quad (2.8)$$

Projection data at a particular angle θ is represented by P_θ . The symbol \tilde{P}_θ represents filtered projection data. The taking of the real part of the integral is denoted by Re .

2.2 Fan-beam reconstruction formula

We will now modify Eqns. 2.7-2.8 for projections from a fan-beam geometry. This is accomplished by a simple change in variables. Changing the scanner configuration from parallel-beam to fan-beam changes the geometry of the system. Fig. 2.2 represents the fan-beam geometry. Rays diverge from a single source located at a distance d from the center of rotation. The rotation angle is represented by Φ . The line segment A represents the detector translated into the center of rotation. In this and the derivations that follow, the detector is assumed to be located in the plane that contains the axis of rotation. The necessary scaling to correct for this assumption is described below when the focus is on implementation issues.

The variables l and θ in Fig. 2.2 are as defined for the parallel-beam geometry. Specifically, to switch geometries to fan-beam, we need to find (Y, Φ) in terms of (l, θ) so that $P_\Phi(Y)$ can be defined. From Fig. 2.2 it can be shown that,

$$Y = \frac{ld}{\sqrt{d^2 - l^2}} \quad (2.9)$$

and

$$\Phi = \theta - \frac{\pi}{2} - \alpha \quad (2.10)$$

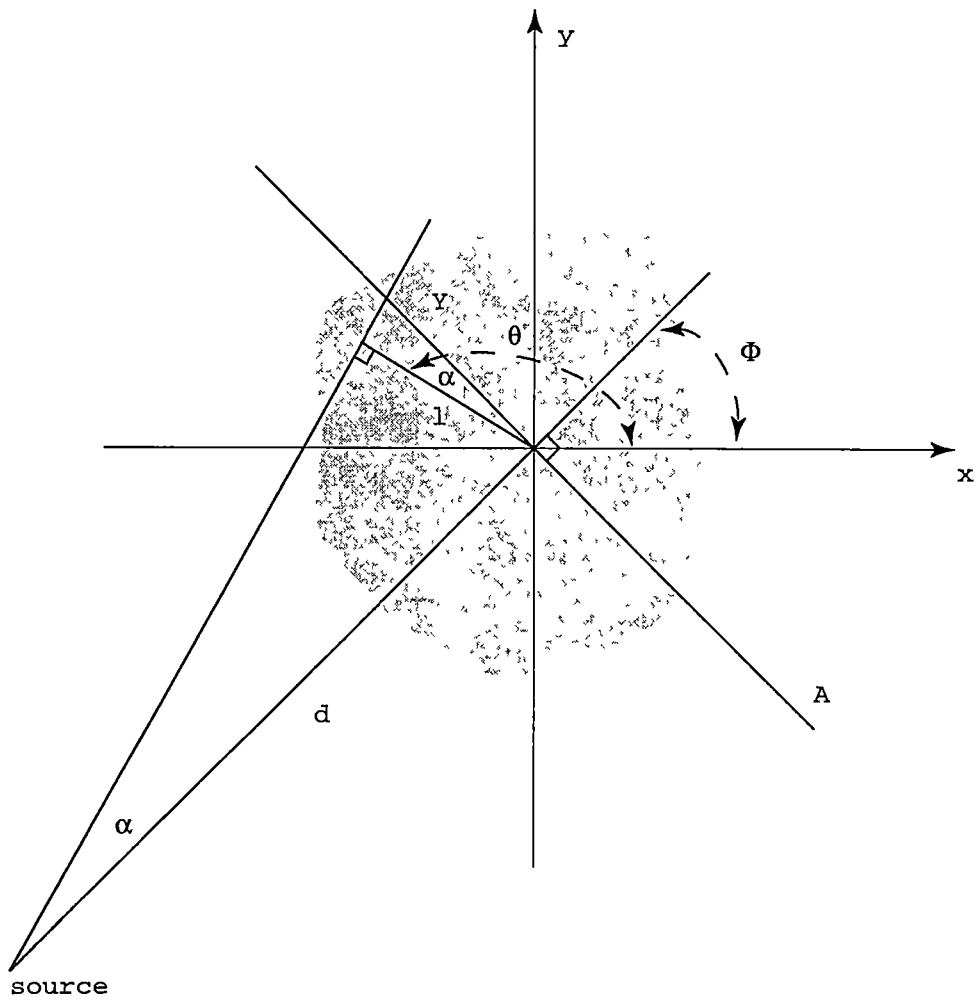


Figure 2.2: Fan beam geometry

Substituting Eqn. 2.8 into 2.7 and a change in variables from (l, θ) to (Y, Φ) such that,

$$d\theta dl = \frac{d^3}{(d^2 + Y^2)^{\frac{3}{2}}} d\Phi dY \quad (2.11)$$

gives us,

$$f(r, \phi) = \frac{1}{4\pi^2} \text{Re} \int_0^{2\pi} \frac{d^2}{[d + r \cos(\phi - \Phi)]^2} \int_0^\infty \omega \int_{-\infty}^\infty \frac{d}{\sqrt{d^2 + Y^2}} P_\Phi(Y(r, \phi)) \exp i\omega[r \cos(\theta - \Phi) - l] dY d\omega d\Phi \quad (2.12)$$

Scaling the frequency ω provides a further convenient change in variables,

$$\omega' = \omega \frac{d + r \cos(\phi - \Phi)}{\sqrt{d^2 + Y^2}} \quad (2.13)$$

which leads to the final form,

$$f(r, \phi) = \frac{1}{4\pi^2} \text{Re} \int_0^{2\pi} \frac{d^2}{[d + r \cos(\phi - \Phi)]^2} \int_0^\infty \omega' \int_{-\infty}^\infty \frac{d}{\sqrt{d^2 + Y^2}} P_\Phi(Y(r, \phi)) \exp \left[i\omega' \left(\frac{dr \sin(\phi - \Phi)}{d + r \cos(\phi - \Phi)} - Y \right) \right] dY d\omega' d\Phi \quad (2.14)$$

2.3 Cone-beam reconstruction formula

We are now in a position to develop the Feldcamp algorithm for cone-beam reconstructions by a heuristic extension of Eqn. 2.14 to three-dimensions. The development will proceed as follows. Starting with points in the midplane, we can determine the incre-

mental contribution to f from g for a small rotation of θ since its geometry reduces to that of fan-beam. Moving out from the midplane, we consider the diverging fan-beams as defining a set of tilted planes. The Feldcamp algorithm is based on an assumption that if we treat the tilted planes as the midplanes of new coordinate systems, we can calculate their contributions to the reconstruction by using Eqn. 2.14 while correcting for the geometric differences.

Consider an object centered at the origin of a three-dimensional coordinate system and along the z -axis. As we have seen in Chapter 1 (Figs 1.1–1.2), the geometry of the midplane, $z = 0$ of such a system reduces to that of the fan-beam case. A point source located on the midplane and rotated around the z -axis at a fixed distance d will describe a set of fans in the midplane whose projections through the object are sufficient to reconstruct the center slice of that object. Therefore, from Eqn. 2.14 the center slice is (dropping the prime from ω'),

$$f(x, y, z = 0) = \frac{1}{4\pi^2} \text{Re} \int_0^{2\pi} \frac{d^2}{(d + (x, y, z = 0) \cdot \hat{x}_\Phi)^2} \int_0^\infty \omega \int_{-\infty}^\infty \frac{d}{\sqrt{d^2 + Y^2}} P_\Phi(Y, Z = 0) \exp \left[i\omega \left(\frac{d((x, y, z = 0) \cdot \hat{y}_\Phi)}{d + (x, y, z = 0) \cdot \hat{x}_\Phi} - Y \right) \right] dY d\omega d\Phi \quad (2.15)$$

We have switched to a vector notation in order to aid in the geometric interpretation of the derivation and to simplify the notation.

Now consider the tilted fan-beams that intersect points in the object not in the midplane as shown in Fig. 2.3. Each fan-beam lies in a unique plane spanned by unit

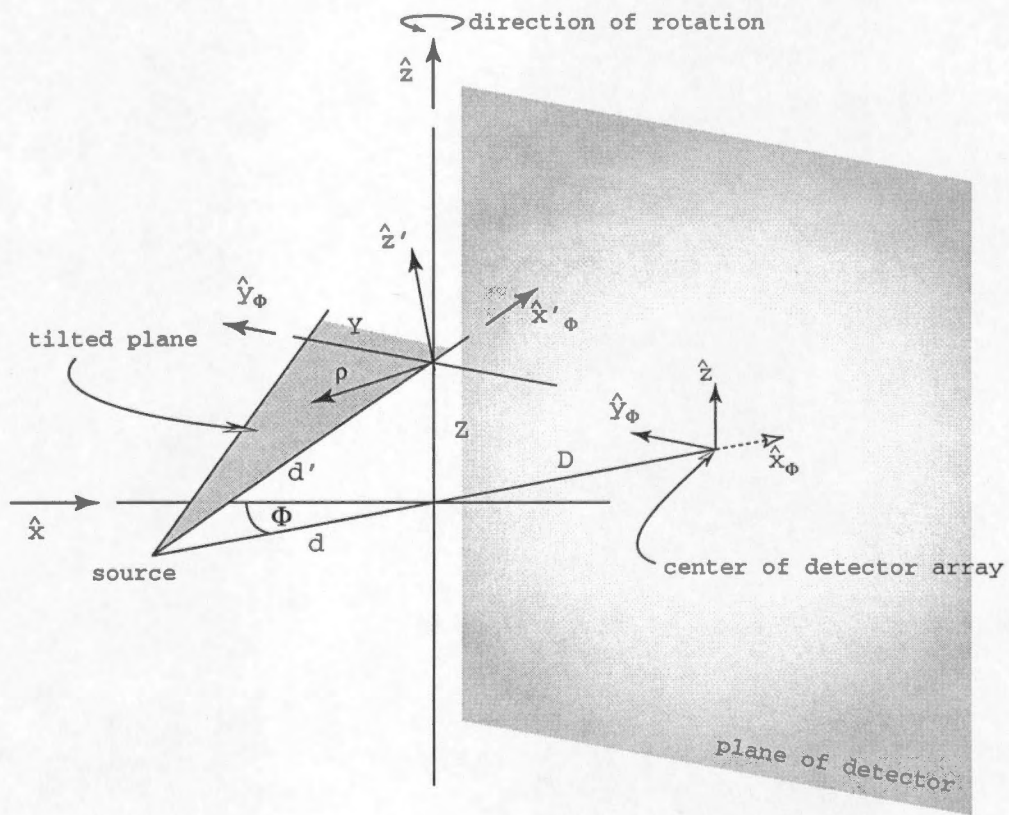


Figure 2.3: Cone-beam geometry. Note that in the derivation, $D = 0$.

vectors \hat{x}'_{Φ} and \hat{y}_{Φ} , where \hat{x}'_{Φ} points along the ray from the source to the detector at $(Y = 0, Z)_{\Phi}$ and \hat{y}_{Φ} points along the Y direction. The vectors \hat{x}'_{Φ} , \hat{y}_{Φ} , and $z' = \hat{x}'_{\Phi} \times \hat{y}_{\Phi}$ define the axes of a new coordinate system. This new coordinate system has its origin translated up the z axis and has been tilted with respect to x_{Φ} . Translating and tilting the coordinate system in this way changes the source to origin distance d and changes the magnitude of the incremental change in the angle of rotation $\delta\Phi$. (The detector plane in Fig. 2.3 is shown translated distance D out of the center of rotation, which is its true location. The derivation assumes that $D = 0$ so that the detector plane is in the center of rotation.)

From Fig. 2.3, the source to origin distance of the new coordinate system is,

$$d' = \sqrt{d^2 + Z^2} \quad (2.16)$$

To find the corresponding incremental change $\delta\Phi'$ for the new coordinate system note that since angular momentum in the system must be conserved,

$$\delta\Phi' d' = \delta\Phi d \quad (2.17)$$

It follows from Eqs. 2.16 and 2.17 that,

$$\delta\Phi' = \frac{\delta\Phi d}{\sqrt{d^2 + Z^2}} \quad (2.18)$$

The contribution to the reconstructed volume for a tilted coordinate system has now

been found. From Eqns. 2.15, 2.16, and 2.18,

$$\delta f(\vec{\rho} + Z\hat{z}) = \frac{1}{4\pi^2} \frac{d'^2}{(d' + \vec{\rho} \cdot \hat{x}_\Phi)^2} \delta\Phi' \int_0^\infty \omega \int_{-\infty}^\infty \frac{d'}{\sqrt{d'^2 + Y^2}} P_\Phi(Y, Z) \exp \left[i\omega \left(\frac{d'(\vec{\rho} \cdot \hat{y}_\Phi)}{d' + \vec{\rho} \cdot \hat{x}_\Phi} - Y \right) \right] dY d\omega \quad (2.19)$$

Vector $\vec{\rho}$ is in the plane defined by the tilted fan. Vector $\vec{\rho}$ extends from the origin of the tilted coordinate system to the reconstruction point. Z is the projected height of $\vec{\rho}$ on the detector array. From Fig. 2.3

$$Z = \frac{\hat{z}d}{d + \vec{r} \cdot \hat{x}_\Phi} \quad (2.20)$$

where \vec{r} is an arbitrary reconstruction point and can be written as,

$$\vec{r} = \vec{\rho} + Z\hat{z} \quad (2.21)$$

To change from $\vec{\rho}$ to \vec{r} in Eqn. 2.19 observe that from Fig. 2.3 the \hat{x}'_Φ component of $\vec{\rho}$ is equivalent to the \hat{x}_Φ component of \vec{r} scaled by the cosine of the angle between \hat{x}_Φ and \hat{x}'_Φ ,

$$\vec{\rho} \cdot \hat{x}'_\Phi = \frac{d'}{d} (\vec{r} \cdot \hat{x}_\Phi) \quad (2.22)$$

and because the tilt of the plane is on the \hat{y}_Φ axis, the \hat{y}_Φ components of the two vectors

are equivalent,

$$\vec{\rho} \cdot \hat{y}_\Phi = \vec{r} \cdot \hat{y}_\Phi \quad (2.23)$$

From Eqns 2.16–2.17 and 2.22–2.23,

$$\delta\Phi' \frac{d'}{\sqrt{d'^2 + Y^2}} = \delta\Phi \frac{d}{\sqrt{d^2 + Y^2 + Z^2}} \quad (2.24)$$

$$\frac{d'^2}{(d' + \vec{\rho} \cdot \hat{x}'_\Phi)^2} = \frac{d'^2}{(d' + \frac{d'}{d}(\vec{r} \cdot \hat{x}_\Phi))^2} \times \frac{\frac{d^2}{d'^2}}{\frac{d^2}{d'^2}} = \frac{d^2}{(d + \vec{r} \cdot \hat{x}_\Phi)^2} \quad (2.25)$$

$$\frac{d'(\vec{\rho} \cdot \hat{y}_\Phi)}{d' + \vec{\rho} \cdot \hat{x}'_\Phi} = \frac{d'(\vec{r} \cdot \hat{y}_\Phi)}{d' + \frac{d'}{d}(\vec{r} \cdot \hat{x}_\Phi)} \times \frac{\frac{d}{d'}}{\frac{d}{d'}} = \frac{d(\vec{r} \cdot \hat{y}_\Phi)}{d + \vec{r} \cdot \hat{x}_\Phi} \quad (2.26)$$

Substituting Eqns. 2.24–2.26 into 2.19 gives the contribution for any reconstruction point \vec{r} ,

$$\begin{aligned} \delta f(\vec{r}) = \frac{1}{4\pi^2} \delta\Phi \frac{d'^2}{(d + \vec{r} \cdot \hat{x}_\Phi)^2} \int_0^\infty \omega \int_{-\infty}^\infty \frac{d}{\sqrt{d^2 + Y^2 + Z^2}} \\ P_\Phi(Y, Z) \exp \left[i\omega \left(\frac{d(\vec{r} \cdot \hat{y}_\Phi)}{d + \vec{r} \cdot \hat{x}_\Phi} - Y \right) \right] dY d\omega \end{aligned} \quad (2.27)$$

Summing Eqn. 2.27 over all projection angles gives us the final form of the Feldkamp algorithm,

$$f(\vec{r}) = \frac{1}{4\pi^2} \int_0^{2\pi} \frac{d^2}{(d + \vec{r} \cdot \hat{x}_\Phi)^2} \tilde{P}_\Phi[Y(\vec{r}), Z(\vec{r})] d\Phi \quad (2.28)$$

where,

$$Y(\vec{r}) = \frac{\vec{r} \cdot \hat{y}_\Phi d}{d + \vec{r} \cdot \hat{x}_\Phi} \quad (2.29)$$

$$Z(\vec{r}) = \frac{\vec{r} \cdot \hat{z} d}{d + \vec{r} \cdot \hat{x}_\Phi} \quad (2.30)$$

$$\tilde{P}_\Phi(Y, Z) = \int_{-\infty}^{\infty} \int_{-\infty}^{\infty} g_y(Y - Y') g_z(Z - Z') P_\Phi(Y', Z') \frac{d}{\sqrt{d^2 + Y'^2 + Z'^2}} dY' dZ' \quad (2.31)$$

$$g_y(Y) = \text{Re} \int_0^{\pi/\Delta Y} \omega \exp(i\omega Y) d\omega \quad (2.32)$$

$$g_z(Z) = \frac{\sin \pi Z / \Delta Z}{\pi Z} \quad (2.33)$$

Eqn.2.31 is the convolution filtering step Eqn.2 28 is the backprojection step. Because detector spacings ΔY and ΔZ are finite, bandlimiting is introduced in Y and Z . Integration over ω is limited to $0 < \omega < \pi/\Delta Y$ because the frequency cannot exceed $\pi/\Delta Y$. Bandlimiting in Z is modeled by convolving $\tilde{P}_\Phi(Y(\vec{r}), Z)$ with the *sinc* function (Eqn 2.33).

It is easy to show that the Feldkamp equations reduce to the parallel-beam case as $d \rightarrow \infty$. As in the fan-beam case, the reconstruction in the midplane is exact. Because the heuristic assumption on which the algorithm is based is only an approximation, off-midplane distortions occur. An analysis of these distortions can be found in [2]. Any further inaccuracies in the Feldkamp algorithm are due to violation of the completeness

condition.

2.4 Data completeness and the generalized Feldkamp formula

We will now talk about the completeness condition and explain how the Feldkamp algorithm can be extended to satisfy it. In order to obtain an exact reconstruction, data must be measured from a sufficient number of perspectives. The completeness condition for cone-beam tomography defines criteria for source trajectories that acquire sufficient (complete) data. The definition of complete data varies to some extent with the reconstruction method used since the formula which inverts $\mathcal{R}f$ specifies what information needs to be obtained to undo that inversion. Here we will use the condition established by Tuy [14] since it is easily described and, like Feldkamp, is based on Radon inversion. Cone-beam methods developed by others have defined various restrictions and generalizations of Tuy's condition. A good review of the history of data sufficiency theory can be found in [1]

As defined by Tuy's Radon inversion technique, an orbit (source trajectory) for data sufficiency must satisfy the following condition: *All planes intersecting some region of interest (ROI) must contain a point on the orbit in order for the ROI to be reconstructed exactly.* Because the most common ROI in the MicroCAT scanner is the entire mouse, the condition becomes: *All planes intersecting the object must contain a point on the orbit in order to have complete information about the object.* This latter statement will

serve for the purposes of the following discussion, but it is important to note that it is a more restrictive condition.

The Feldkamp algorithm is for data collected from a circular source orbit. But a circular orbit clearly does not satisfy the completeness condition. In fact, a circular orbit only provides complete data for those points on the midplane of the object. No plane parallel to the midplane contains a point on the orbit, for example. If we can extend Feldkamp for data collected from an orbit that is sufficient (satisfies the completeness condition), then we can improve the accuracy of our reconstructions. Wang et al. [16] have proposed a generalized cone-beam algorithm based on the Feldkamp method that allows for arbitrary orbits by letting the parameters that describe the source location vary.

The Wang method follows the same heuristic development as the Feldkamp algorithm with two important differences. The first difference is that the midplane is no longer fixed at the center of the reconstruction area $z = 0$, but is allowed to move up and down the z axis. The second change is that the source-to-origin distance d also becomes variable. These two generalizations allow for arbitrary source trajectories.

To implement these generalizations we define a reference coordinate plane at $z = 0$ to be equivalent to what was formerly the midplane of our system. Then we redefine the locus of the x-ray source as,

$$(d(\Phi), h(\Phi), \Phi) \tag{2.34}$$

where $d(\Phi)$ is the source-to-origin distance at angle Φ , $h(\Phi)$ is the vertical distance from the source to the reference plane, and $\Phi \in [0, 2\pi]$ as before.

Substituting 2.34 into Eqn. 2.27 and summing over all projection angles we have,

$$f(\vec{r}) = \frac{1}{4\pi^2} \int_0^{2\pi} \frac{d(\Phi)^2}{(d(\Phi) + \vec{r} \cdot \hat{x}_\Phi)^2} \int_0^\infty \omega \int_{-\infty}^\infty \frac{d(\Phi)}{\sqrt{d(\Phi)^2 + Y^2 + \zeta^2}} P_\Phi(Y, \zeta) \exp \left[i\omega \left(\frac{d(\vec{r} \cdot \hat{y}_\Phi)}{d(\Phi) + \vec{r} \cdot \hat{x}_\Phi} \right) \right] dY d\omega d\Phi \quad (2.35)$$

with,

$$\zeta = \frac{d(\Phi)\tilde{z}(\Phi)}{d(\Phi) + \vec{r} \cdot \hat{x}_\Phi} \quad (2.36)$$

$$\tilde{z}(\Phi) = z - d(\Phi) \quad (2.37)$$

which represents the generalized Feldkamp algorithm.

We will now turn our focus from the theory behind volumetric reconstruction techniques, to the actual implementation in the MicroCAT system of such a method. This section has described the Feldkamp cone-beam algorithm and a logical extension of that algorithm to facilitate higher quality reconstructions through sufficient orbits. The next chapter will describe how the Feldkamp algorithm can be discretized and its implementation, including angular scanning limitations and the algorithmic attempts to overcome them.

Chapter 3

Implementation issues

This chapter will talk about how a volumetric algorithm was implemented in the MicroCAT system and the issues that surround that implementation. The discussion is organized as follows. First, a discrete approximation of the Feldkamp algorithm is made. Then, a computer implementation of the algorithm is described. Next, compensation schemes are discussed to help overcome the angular scanning limitations of the MicroCAT system. This chapter concludes with a brief discussion of a future implementation for a helical scanning geometry and parallelization of the algorithm.

3.1 Discretized Feldkamp

In practice, we can only record a finite number of projections and each projection can only be sampled at a finite number of points. So we assume that sampling is at equally spaced intervals and average around those points. The discretized data is represented

as $P_{\Phi_i}(Y_j, Z_k)$, where $\Delta\Phi = \Phi_i - \Phi_{i-1}$, $\Delta Y = Y_j - Y_{j-1}$, and $\Delta Z = Z_k - Z_{k-1}$. From Eqn. 2.31, filtered data for projection i becomes,

$$\begin{aligned} \tilde{P}_{\Phi_i}(Y_j, Z_k) = & \sum_{j', k'} P_{\Phi_i}(Y_{j'}, Z_{k'}) \frac{d}{\sqrt{d^2 + Y_{j'}^2 + Z_{k'}^2}} \\ & \int_{Y_{j'} - \Delta Y/2}^{Y_{j'} + \Delta Y/2} g_y(Y_j - Y') dY' \int_{Z_{k'} - \Delta Z/2}^{Z_{k'} + \Delta Z/2} g_z(Z_k - Z') dZ' \quad (3.1) \end{aligned}$$

The integrals in Eqn. 3.1 accomplish the averaging around the data points and describe the convolution filtering kernels. Note that the discrete convolution filtering separates into two, one-dimensional convolutions. Thus, filtering can be done separately in the Y and Z directions. This is beneficial for the implementation because it reduces the computational complexity of the filtering process from an order n^2 process to order $2n$.

To complete the reconstruction, Eqns 2.28–2.30 are used to backproject the filtered data into reconstruction points \vec{r} . The integral in Eqn. 2.28 is replaced with a summation of values over all projection angles Φ_i .

Though discretized, Eqn. 3.1 is not yet in a form that is practical to implement. It is computationally expensive due to the integrals it contains (numerical integration would be required). Fortunately, we can find closed-form solutions to those integrals as follows. Performing the integration in Eqn. 2.32 gives us,

$$g_y(Y) = \text{Re} \left[\frac{i\omega_{y_0} Y e^{i\omega_{y_0} Y} - e^{i\omega_{y_0} Y} + 1}{-Y^2} \right] \quad (3.2)$$

where ω_{y_0} is the maximum frequency limitation $\pi/\Delta Y$ due to the detector spacing

Substituting $e^{i\omega_{y_0} Y} = \cos(\omega_{y_0} Y) + i \sin(\omega_{y_0} Y)$ and taking the real part of the result gives us,

$$g_y(Y) = \frac{\omega_{y_0} Y \sin(\omega_{y_0} Y) + \cos(\omega_{y_0} Y) - 1}{Y^2} \quad (3.3)$$

Using the result for $g_y(Y)$ we can solve the integral

$$h(Y_j) = \int_{Y_j' - \Delta Y/2}^{Y_j' + \Delta Y/2} g_y(Y_j - Y') dY' \quad (3.4)$$

by changing variables so that $\alpha = Y_j - Y'$ and $d\alpha/dY' = -1$ and integrating from $a = Y_j - Y_j' - \Delta Y/2$ to $b = Y_j - Y_j' + \Delta Y/2$ to produce

$$h(Y_j) = - \int_a^b \frac{\omega_{y_0} \alpha \sin(\omega_{y_0} \alpha)}{\alpha^2} d\alpha - \int_a^b \frac{\cos(\omega_{y_0} \alpha)}{\alpha^2} d\alpha + \int_a^b \frac{1}{\alpha^2} d\alpha \quad (3.5)$$

Substituting

$$\int_a^b \frac{\cos(\omega_{y_0} \alpha)}{\alpha^2} d\alpha = \left[\frac{\cos(\omega_{y_0} \alpha)}{\alpha} \right]_a^b - \omega_{y_0} \int_a^b \frac{\sin(\omega_{y_0} \alpha)}{\alpha} d\alpha \quad (3.6)$$

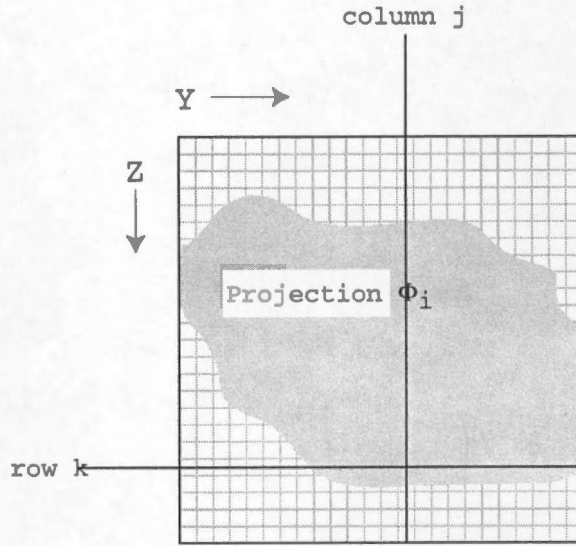


Figure 3.1: A matrix of projection data

into Eqn. 3.5 and integrating produces,

$$h(Y_j) = \frac{\cos(\omega_{y_0}(Y_j - Y_{j'} + \Delta Y/2)) - 1}{Y_j - Y_{j'} + \Delta Y/2} + \frac{1 - \cos(\omega_{y_0}(Y_j - Y_{j'} - \Delta Y/2))}{Y_j - Y_{j'} - \Delta Y/2} \quad (3.7)$$

Eqn. 3.7 describes the convolution kernel used to filter data in the Y direction. Fig. 3.1 shows the arrangement of a matrix of projection data at some angle Φ_i . Rows Y_k of the matrix represent the one-dimensional arrays of data in the Y direction. For each row in the matrix, convolution filtering is performed as $P_{\Phi_i, Y_k}(j) * h(j)$ where,

$$h(j) = \frac{\cos(\omega_{y_0}(j + \Delta Y/2)) - 1}{j + \Delta Y/2} + \frac{1 - \cos(\omega_{y_0}(j - \Delta Y/2))}{j - \Delta Y/2} \quad (3.8)$$

Analysis of the Z -directional (axial) filtering allows us to make a further reduction in

computational complexity. If we disregard the averaging in the axial direction, replacing the last integral in Eqn. 3.1 by $g_z(Z_k - Z_{k'})\Delta Z$ has the net effect of convolving with the *delta* function. We can therefore drop the convolution in the Z direction since it has no effect.

To complete the discrete version of the Feldkamp algorithm, we observe that for a clockwise rotation, $\hat{x}_\Phi = (\cos \Phi, -\sin \Phi, 0)$, $\hat{y}_\Phi = (\sin \Phi, \cos \Phi, 0)$ and $\hat{z} = (0, 0, 1)$. The final form is now given by,

$$f(x, y, z) = \frac{1}{4\pi^2} \sum_i \frac{d^2}{(d + x \cos \Phi_i - y \sin \Phi_i)^2} \tilde{P}_{\Phi_i}[Y(x, y, z), Z(x, y, z)] \quad (3.9)$$

$$Y(x, y, z) = \frac{d(x \sin \Phi_i + y \cos \Phi_i)}{d + x \cos \Phi_i - y \sin \Phi_i} \quad (3.10)$$

$$Z(x, y, z) = \frac{dz}{d + x \cos \Phi_i - y \sin \Phi_i} \quad (3.11)$$

$$\tilde{P}_{\Phi_i}(Y_j, Z_k) = \sum_{j', k'} \frac{d}{\sqrt{d^2 + Y_{j'}^2 + Z_{k'}^2}} P_{\Phi_i}(Y_{j'}, Z_{k'}) h(Y_j - Y_{j'}) \quad (3.12)$$

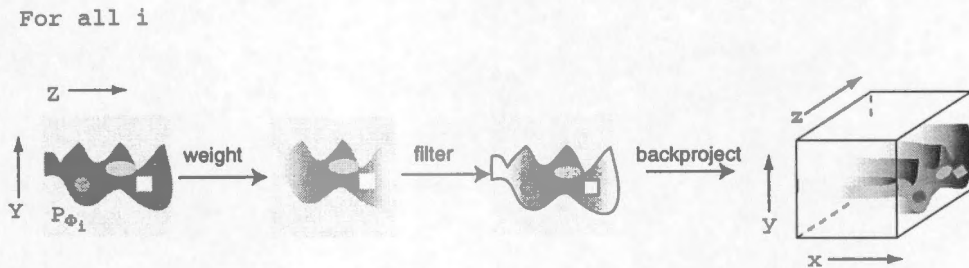


Figure 3.2: Illustration of Feldkamp filtered backprojection algorithm

3.2 Computer implementation

Once the analysis of the algorithm has been done, coding it is a relatively straightforward process. Fig. 3.2 outlines the algorithm. Reconstruction separates into several discrete processes. Data is loaded projection by projection. Each projection is then weighted by the factor $d/\sqrt{d^2 + Y^2 + Z^2}$, filtered, and then its contribution is backprojected into a reconstruction volume.

The weighting of the data is performed by point-wise multiplication with a pre-calculated $Y \times Z$ matrix. The matrix is data-independent. It is based solely on the scanning geometry. Elements of the matrix are the cosines of the angles between diverging rays from the source to detector coordinates ($Y \neq 0, Z \neq 0$) and the ray from the source to ($Y = 0, Z = 0$) (see Fig. 2.3). Points close to the center of the matrix have values close to one, points at increasing distance from the center are diminished at a rate proportional to the cone-angle. As d is increased, the cone-angle becomes smaller and the weighting has less and less impact. As $d \rightarrow \infty$, the weighting disappears altogether (parallel case).

The convolution filtering of the data in the Y direction is done with a pre-calculated filter kernel. The filtering kernel, like the weight matrix, is based solely on the scanner geometry. The full width of the kernel is not used. Using the full width of the kernel makes the filtering process much too slow. The size of the kernel determines the degree of filtering. Thus there is a tradeoff between speed of reconstruction and the amount of detail that the filtering resolves. Filtering using the full width of the kernel is more quickly done in the frequency domain.

The filter is a derivative filter similar to the Shepp-Logan window [2]. Low frequencies in the image (background) are filtered out, leaving the high-frequencies (edges). There is a degree of roll-off at the extremes of the filtering window to minimize the effects of a sharp cutoff (Gibbs phenomena).

Filtering was also implemented in the frequency domain using both a ramp filter with discrete impulse response,

$$h(j) = \begin{cases} \frac{-1}{\pi^2 \sin^2(j\Delta Y)}, & j, \text{ odd} \\ 0, & j, \text{ even } j \neq 0 \\ \frac{1}{4\Delta Y^2}, & j = 0 \end{cases} \quad (3.13)$$

and a Shepp-Logan window with discrete impulse response,

$$h(j) = \frac{2}{\pi^2 \Delta Y^2 (1 - 4j^2)} \quad (3.14)$$

Frequency domain filtering was accomplished by taking the discrete, fast Fourier trans-

form of rows (Y -direction) of projection data and multiplying by the filtering window. Frequency domain filtering has the advantage that the full width of the filtering kernel is used, but is slower than convolution filtering with small kernels. The type of filtering used will depend on the application and the desired reconstruction speed. Further analysis of filtering issues is undertaken in the next chapter.

To hold the reconstruction, a volume of arbitrary dimensions is created into which all filtered projections are backprojected. Backprojection is done by looping through the x , y , and z coordinates of the volume and “pulling” the appropriate data into its voxels. This is in contrast to looping through the Y , Z coordinates of the projection data and “pushing” data into the volume. The latter technique has the effect of averaging neighboring data point values and so might seem advantageous in reducing noise and increasing effective detector counts. But, pushing the data requires more computations since each voxel is visited multiple times (versus only once for the pulling method). Additionally, a three-dimensional interpolation is required to locate the voxel in which to push the data, whereas pulling data only requires a two dimensional interpolation. Averaging of neighboring pixels can be done more efficiently by downsampling the projection data prior to processing.

Pulling the data into the reconstruction volume is a process of projecting a reconstruction point out into the detector plane and then interpolating among the four closest integer detector positions (grid-square). Because the derivation of the Feldkamp algorithm assumes that the plane of the detector is translated to the center of rotation, the

projections of the reconstruction points onto the detector array must be scaled accordingly. Specifically, if d is the source-to-center of rotation distance, and D is the source to center-of-detector distance, then Eqns 3 10 and 3 11 are scaled by the value D/d

Two interpolation methods are used in this implementation. The first is to simply truncate the projected detector plane coordinates to integers and use the single value at that location. This method is fast, but sensitive to noise. The second method implemented is bi-linear interpolation on the grid-square which produces a biased average of the points towards the grid-square values closest to the interpolating point. Bi-linear interpolation slows the backprojection down, but produces a better image because it introduces smoothing and noise cancelation by averaging neighboring pixels

Another strategy for smoothing and noise reduction in lower-resolution reconstructions is to first downsample the projection to average neighboring values. Downsampling also has other advantages of reducing filtering time and increasing detector counts. Filtering time is reduced exponentially since its computational complexity is a factor of the image size. Detector counts are effectively increased when neighbor points are summed during downsampling, and may be important if detector counts have been sacrificed for speed during the scanning process.

Downsampling was implemented using the heat diffusion equation given by [17]

$$\frac{\partial u}{\partial t} = \nabla^2 u$$

$$u(Y, Z, 0) = P(Y, Z) \quad (3.15)$$

where ∇^2 represents the Laplacian operator. The function $u(Y, Z, t)$ describes the diffusion of P after t units of time. Eqn. 3.15 is solved by blurring $P(Y, Z)$ with Gaussian functions of width proportional to t . Solving the equation for increments of t gives a multiscale representation of P where the resolution steps down as t increases. Down-sampling of the image is accomplished by convolving P with a Gaussian function

$$G(Y, Z, t) = 1/4\pi t \exp[-(Y^2 + Z^2)/4t], \quad t > 0 \quad (3.16)$$

of standard deviation $\sqrt{2t}$, and then resampling into an image of size $Y/2^t \times Z/2^t$ by averaging neighbor points.

3.3 Compensation techniques for short-scans

As first noted in Chapter 1, the MicroCAT system cannot rotate further than about 3.4 radians. Because the scanning trajectory is less than 2π , and the Feldkamp algorithm is based on a full circular scan, we must seek a way to compensate for the missing view angles. Reconstruction with missing angles creates an imbalance in the weighting of the ray-sum data as it is backprojected into the image space, resulting in an image that is too dark in those regions closest to the missing trajectory vertices and too bright elsewhere. Other artifacts in the reconstruction result from the fact that some ray-sums are doubly sampled while others are only sampled once. In this section we will discuss

several compensation schemes for scans less than 2π radians (short-scans).

There are many advantages of using a short-scan. Scanning and reconstruction times are both reduced, as well as the exposure time of the specimen to radiation. A shortened scan time can reduce artifacts due to movement of specimen during the scan. Eliminating the need for a full circular trajectory cuts down on hardware cost and complexity. Like the initial development of the Feldkamp algorithm itself, compensations for short-scan data sets are developed heuristically by extending the parallel and fan-beam cases. We first determine the minimum number of views required to sample all possible ray-sums (minimally complete data set), from which we can use the rotational symmetry of the system to compensate for missing ray-sums in several ways

In the parallel-beam case, a minimally complete data set consists of projections $0 \leq \theta < \pi$. It is easy to see that, because the beams are parallel, a full 2π scan in a parallel geometry records each ray-sum through the object exactly twice. Beams from projection 0 line up with those from projection π , for example, producing the same projection image. This is true for any constant α at $0 + \alpha$ and $\pi + \alpha$.

The situation is more complicated for the fan-beam geometry. But fan-beam data can be rebinned into parallel beam data. So to find the minimally complete data set for a fan-beam geometry, we need to find the minimum number of views required to rebin to a parallel geometry with a projection set from $0 \leq \theta < \pi$

Rebinning maps a Radon transform g in fan-beam geometry to a Radon transform p in the parallel-beam geometry. If Φ and α are the projection angle and ray-angle of

the ray-sum in a fan-beam (Fig. 2.2), and θ and l are the projection angle and offset of the ray-sum from a beam in a parallel projection (Fig 2 1), then

$$g(l, \theta) = p(\alpha, \Phi) \quad (3.17)$$

when

$$\theta = \Phi + \alpha \quad (3.18)$$

$$l = d \sin \alpha \quad (3.19)$$

where d is the source-to-center of rotation distance of the fan-beam

From these relationships, with the additional requirement imposed by rotational symmetry,

$$g(l, \theta) = g(-l, \theta + \pi) \quad (3.20)$$

$$p(\alpha, \Phi) = p(-\alpha, \pi + \Phi + 2\alpha) \quad (3.21)$$

we can show that the minimally complete data set for a fan-beam geometry consists of views $0 \leq \Phi < \pi + 2\delta$, where 2δ is the fan-angle

This result is illustrated in Fig 3 3 Fig 3.3(a) is the Radon transform p in a fan-beam geometry. Fig 3.3(b-d) are mappings p into the parallel-beam geometry from

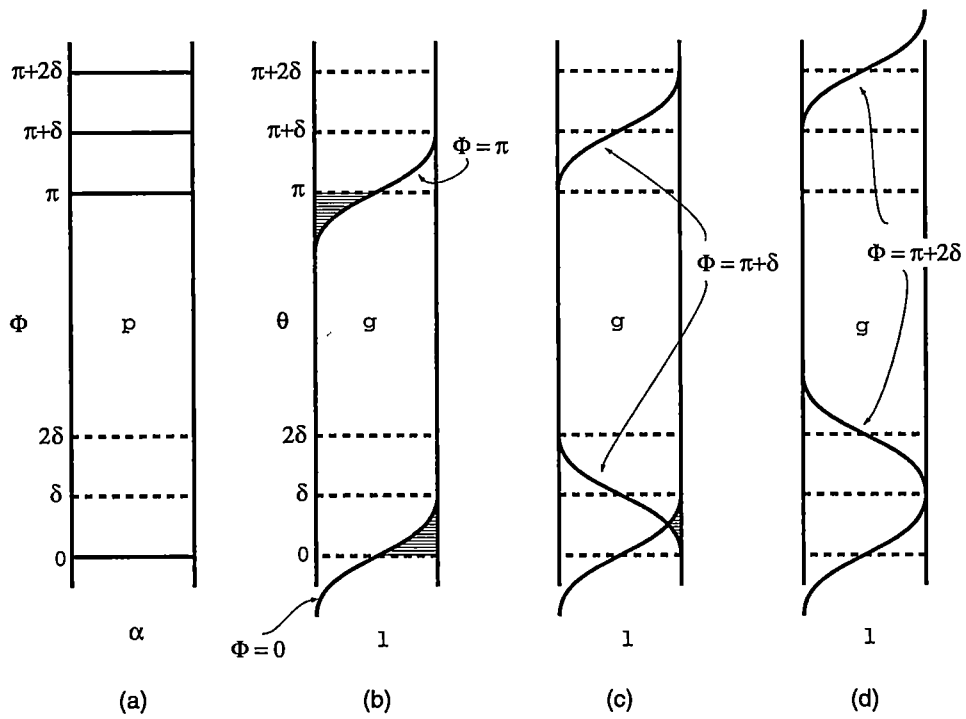


Figure 3.3. Symmetry of and relationship between the minimally complete data sets of the two dimensional Radon transforms of fan-beam acquired data g and parallel-beam data p .

successively more complete scans. The shaded regions between 0 and π represent data that has been seen. Barred regions represent missing data in that range. For a minimally complete data set p , we need to find boundaries for Φ such that all of the range $0 \leq \theta < \pi$ is seen at least once.

Fig. 3.3(b) is the mapping of data from a fan-beam scan of $0 \leq \Phi < \pi$. The mapping of the boundaries $\Phi = 0$ and $\Phi = \pi$ are shown. It is clear that this range does not represent a minimally complete set. The rotational symmetry of the system is such that the symmetric boundary projection angles produce redundant data instead of complementary data. Fig. 3.3(c) shows the mapping of p when the scanning range is increased to $\pi + \delta$. The missing region just below π is covered by the additional angle, and part of the missing region near 0 is covered by symmetry. Fig. 3.3(d) shows that only when the range is extended to a full cone-angle past π is all of the missing data seen.

Theoretically, we should be able to reconstruct an image from a minimally complete fan-beam projection set since all possible ray-sums have been recorded. Several methods based on the rotational symmetry of the scanning geometry were explored for the MicroCAT system. The first two involve pre-weighting the data to factor out the doubly scanned regions. The third method constructs the missing projections from existing projections.

Parker [8] and Wang et al. [15] propose similar pre-weighting schemes in which they attempt to optimize short-scan reconstructions by weighting existing data so that all

ray-sums are effectively seen only once. A weight function is applied prior to filtering and backprojection that removes redundant data in the doubly scanned regions

Fig 3.4 shows the set of ray-sums as a function of the projection angle Φ and the ray angle α over the minimally complete sampling region. By the rotational symmetry of the system (Eqn. 3.21), the upper triangle is a sampling of the same set of ray sums as the lower triangle. Wang's compensation formula uses the simple approach of setting weights in the upper triangle to zero, and weights elsewhere to one. This weight function is highly discontinuous at the triangle boundaries so an additional sampling region Δ past $\pi + 2\delta$ in which weights are transitioned smoothly to zero is required to reduce Gibbs phenomenon artifacts.

Parker's weight function is an earlier, but more sophisticated variation on the Wang function. Rays that are seen once (between the two triangles) are given a weight of one. Rays seen twice are weighted such that the sum of their weights is one. Parker imposes constraints on the function so that discontinuities at the borders of the triangles are minimized, avoiding the need for the additional scan angle Δ . Parker's weight function is given by

$$w(\alpha, \Phi) = \begin{cases} \sin^2\left(\frac{\pi}{4} \frac{\Phi}{\delta - \alpha}\right), & 0 \leq \Phi < 2\delta - 2\alpha \\ 1, & 2\delta - 2\alpha \leq \Phi \leq \pi - 2\alpha \\ \sin^2\left(\frac{\pi}{4} \frac{\pi + 2\delta - \Phi}{\delta + \alpha}\right), & \pi - 2\alpha < \Phi \leq \pi + 2\delta \end{cases} \quad (3.22)$$

MicroCAT cone-beam data is in violation of the completeness condition since it was acquired in a circular orbit. So in order to extend the weighting functions into three-

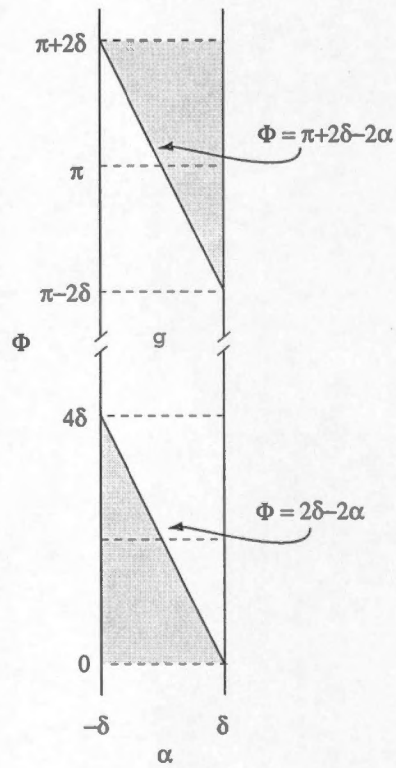


Figure 3.4: Symmetry of the Radon transform g in the range $0 \leq \Phi \leq 2\pi + 2\delta$.

dimensions, we must use an approximation. We can never find a minimally complete set of ray-sums because, out of the midplane of the system, no two rays line up on rotation. We will therefore make an assumption that the rotational symmetry of the data is analogous to the fan beam system,

$$P_{\Phi}(Y, Z) = P_{\beta}(-Y, Z) \quad (3.23)$$

where

$$\beta = \Phi + \pi + 2 \tan^{-1}(Y/d) \quad (3.24)$$

This assumption implies that points in the fan-beam data correspond to columns in the cone-beam data, which is not true, but for small cone-angles is a reasonable approximation. Extension to the Feldkamp algorithm is then an easy matter of applying the weight $w(\alpha_j, \Phi_i)$ to all elements of the corresponding column $P_{\Phi_i}(-\alpha_j, k)$ in the three dimensional system, where α_j is calculated as $\tan^{-1}(Y_j/d)$

The preweighting schemes described above were easily implemented in the Micro-CAT system as an additional processing step for each projection prior to its filtering and backprojection. Additional processing time is minimal compared to filtering and backprojecting times and only applies to those projections containing rays from the triangle regions described in Fig 3.4.

The problem with the methods just described is that they only focus on the back-projection step of the reconstruction algorithm. The divergent beam algorithms are

not just a backprojection of ray-sums, they are weighted and filtered backprojections of ray-sums. In practice, however, the Parker and Wang methods do provide significant improvement in image quality by creating more accurate backprojections.

To address the artifacts introduced by the short-scan during the weighting process, we note that the backprojection weighting in the fan-beam algorithm is a function of the projection angle and is independent of the data. Each ray-sum through the object is measured twice during a full rotation around the object, but the algorithm weights the same ray-sum differently as it is smeared across the image plane from the symmetric angle. The contribution of a ray-sum to a reconstruction point varies inversely with the reconstruction point's distance from the ray source. A reconstruction of a minimally-complete data set, where the source sweeps around only half of the object, therefore results in an image whose intensities are imbalanced. Specifically, an underweighting occurs over half of the image and an overweighting over the opposite half. The underweighting in the image f is in the regions spanned by the angles ϕ of the missing projections, where f is in polar coordinates (r, ϕ) . The overweighting occurs in the remaining regions for which projections exist.

The weighting imbalance is illustrated by Fig. 3.5. Fig. 3.5(a) depicts the relative weights for $\Phi = 0.07$ radians (an arbitrary angle) backprojected onto the image plane of the central slice ($z = 0$) of the reconstruction volume. The arrow shows the direction of the rotation of the source. Ray-sums backprojected into reconstruction points closest to the source are given the highest weights. As Φ increases, the bright and dark regions

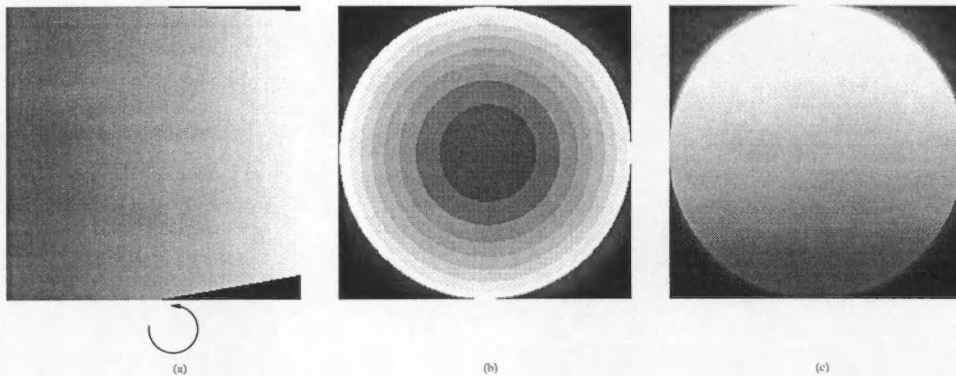


Figure 3.5: Weighting imbalance in the reconstructed image from backprojection over a minimally complete set of angles

sweep around to produce Fig. 3.5(b), the relative weights backprojected over the full 2π radius. When $0 \leq \Phi < \pi$, 3.5(c) is obtained, which shows the relative underweighting of the bottom half of the image and overweighting at the top half. The banding effect in (b) is the result of quantizing a larger range of values than in (a,c) into a 256 graylevel image. The black regions in (a-c) are areas outside the spread of the cone beam and therefore have weight zero.

A simple heuristic correction for the weighting imbalance in the fan-beam case is to weight each singly-sampled ray-sum twice as it is backprojected into a reconstruction point. For a given point (r, ϕ) , weight $P_\Phi(Y(r, \phi))$ once with weights calculated from angles Φ , and again with weights calculated from the symmetric angles $\Phi + \pi + 2\alpha$. Using this method, redundant data does not need to be corrected for.

Using the approximate cone-beam symmetry from Eqn. 3.23, the symmetric-weighting

method applied to the Feldkamp algorithm is given as

$$f(x, y, z) = \frac{1}{4\pi^2} \int_0^{\pi+2\delta} \left(\frac{d^2}{(d+x\cos\Phi-y\sin\Phi)^2} + w(x, y, \Phi) \right) \tilde{P}[Y(x, y, z), Z(x, y, z)] d\Phi \quad (3.25)$$

where

$$w(x, y, \Phi) = \begin{cases} \frac{d^2}{(d+x\cos\beta-y\sin\beta)^2}, & 2\delta - 2\tan^{-1}(Y/d) < \Phi \\ 0, & \text{otherwise} \end{cases} \quad (3.26)$$

The symmetric-weighting technique was implemented for the MicroCAT by calculating and applying the second weight during the backprojection step, which does not cause a significant increase in processing time. In practice, this method provides better weighting compensation than the Parker and Wang techniques, but it introduces more artifacts in the filtering process and so does not necessarily yield a better image. These artifacts come from an assumption that filtered data is symmetric. But it can be seen from Fig. 3.4 that filtering in the α (Y) direction destroys the symmetry given in Eqn. 3.21. Symmetric ray-sums are no longer guaranteed to have the same values once filtered because the filtered value at a point depends on the values of its neighbors, which are different in the symmetric projection. This can be seen by noting that neighbor ray-sums in a single projection (α, Φ_k) , k , constant, correspond by symmetry to ray-sums across multiple projections $(-\alpha, \pi + \Phi_k + 2\alpha)$.

To compensate for a short-scan in all steps of the reconstruction, the missing projections can be created using the assumed symmetry of the system. Once created, they can

be correctly filtered and a full backprojection over 2π radians can be performed. This method is computationally much slower than the previous compensations described, but produces a more accurate image.

In the MicroCAT system, this technique was implemented by again assuming the symmetry given by Eqn 3.23 and then copying columns from existing projections into their symmetric columns in the missing projections. Once the missing projections are created, the Feldkamp algorithm can be run without modification on the full data set. Creating the missing projections is a slow process because of the overhead required to repeatedly index into disparate areas of the large volume of data. A more complete analysis of the effectiveness of all the compensation techniques just described, and a discussion of the trade-off between their reconstruction speed and quality is provided in the next chapter.

3.4 Further enhancements

As discussed in Chapter 2, the Feldkamp algorithm is extensible to geometries that satisfy the completeness condition. For a rod-shaped specimen like a mouse, a helical trajectory is ideal [1] and relatively easy to implement in a third-generation scanner. It is easy to see that all planes intersecting the specimen will intersect a vertex on a helical orbit. Thus Tuy's completeness condition is satisfied. A helical orbit has a fixed source-to-origin distance, $d(\Phi) = d_0$. The z translation is defined as

$$h(\Phi) = \frac{h_p \Phi}{2\pi} \quad (3.27)$$

where h_p is the pitch of the helix turn. Substituting into Eqns. 2.35–2.37 and accounting for bandlimiting as in Eqn. 2.32–2.33 gives the modified Feldkamp cone-beam algorithm for a helical orbit.

For the MicroCAT system, a hardware implementation of a helical geometry would require a simultaneous rotation of the source around the object and translation of the object in the z direction. In the software, the filtering and weighting steps of the reconstruction algorithm are unaffected because the source-to-origin distance $d(\Phi)$ is constant. Only a simple modification in the backprojection is needed to compensate for the translation of the origin up and down the z axis.

A final footnote to the implementation process is that because filtering, weighting, and backprojecting proceed independently from projection to projection without regard to projection order, the algorithm is easily parallelized. From Eqn. 3.9,

$$f = \frac{1}{4\pi^2} \left(w_0 \tilde{P}_{\Phi_0}[Y, Z] + w_1 \tilde{P}_{\Phi_1}[Y, Z] + w_2 \tilde{P}_{\Phi_2}[Y, Z] + \dots + w_n \tilde{P}_{\Phi_n}[Y, Z] \right) \quad (3.28)$$

with

$$w_i = \frac{d^2}{(d + x \cos \Phi_i - y \sin \Phi_i)^2} \quad (3.29)$$

and n the number of projections.

Theoretically, a linear increase in speed could be achieved as the number of processors used approaches n . Parallelizing the Feldkamp algorithm is a simple matter of independently processing each projection into a sub-volume and then summing the sub-volumes into a final image, as in Eqn. 3.28.

While the Feldkamp algorithm was not parallelized for the MicroCAT system, Laurent et al. [7] describe several parallel implementations of the Feldkamp algorithm that are not specific to any particular architecture. They report Feldkamp as the most efficient parallel implementation over several other reconstruction techniques tested, and propose the use of a workstation network for practicing tomographic sites as giving the best price-to-performance tradeoff.

In this chapter, the implementation of the Feldkamp algorithm in the MicroCAT system was explained. It was shown that the implementation requires choices as to the best filtering methods, the best data sampling methods, and the best way in which to compensate for scanning trajectory limitations of the MicroCAT system. The next chapter will compare the effectiveness of the various methods using reconstructed images from MicroCAT data, and will compare Feldkamp reconstructed images with images obtained using the current method.

Chapter 4

Experimental results

This chapter presents an analysis of the Feldkamp algorithm implementation. It begins with a comparison of the compensation weighting schemes for short-scan data sets. The effectiveness of convolution filtering using different sized filter kernels is then demonstrated and compared with the ramp and Shepp-Logan filters applied in the frequency domain. Next, the effects of downsampling the projection data and of the bi-linear interpolation method are shown. Using the best combination of parameters, a Feldkamp reconstruction is compared at increasing axial distances to a reconstruction done with the current method. A discussion of reconstruction times concludes this chapter.

There were two different data sets used for the reconstructions. The first data set is a low resolution (195 projections) scan of a phantom object. The phantom object is a Lucite cylinder with embedded aluminum pins running along the its long axis of the cylinder, one large pin at in the center and several smaller pins spaced at intervals

along an arc in the top half of the cylinder. The cylinder also has two large holes drilled through its length. The x-ray attenuation coefficients of Lucite and aluminum are similar to those of soft tissue and bone, respectively. The second data set is a high resolution (391 projections) scan of the mid-section of a mouse. Both scans were made over an angular range of 0 to π + one full cone-angle of 0.198 radians, the range previously defined as sampling a minimally complete data set. The source-to-detector distance D was approximately 248 cm and the source-to-center-of-rotation distance d was approximately 181 cm.

In many of the images that follow there are distinctive, horizontal streaking artifacts across the middle of the reconstruction circle that resemble scratches. These artifacts are a direct result of the edge of the specimen bed passing in and out of the field of view as the source was rotated. If part of an object is not consistently within the field of view, its contributions to the reconstruction volume from one angle are not appropriately balanced by those from other angles, which results in the streaking just described. Increasing d so that the entire bed remains in view as the source is rotated eliminates these artifacts entirely.

All of the reconstructions shown are from volumes of dimension $256 \times 256 \times 256$ pixels, one quarter of the full projection resolution. For images in which histogram specification was used to spread the graylevels, the same graylevel map was used in each image to ensure an accurate comparison.

Fig 4.1 compares the effectiveness of the various short-scan compensation techniques

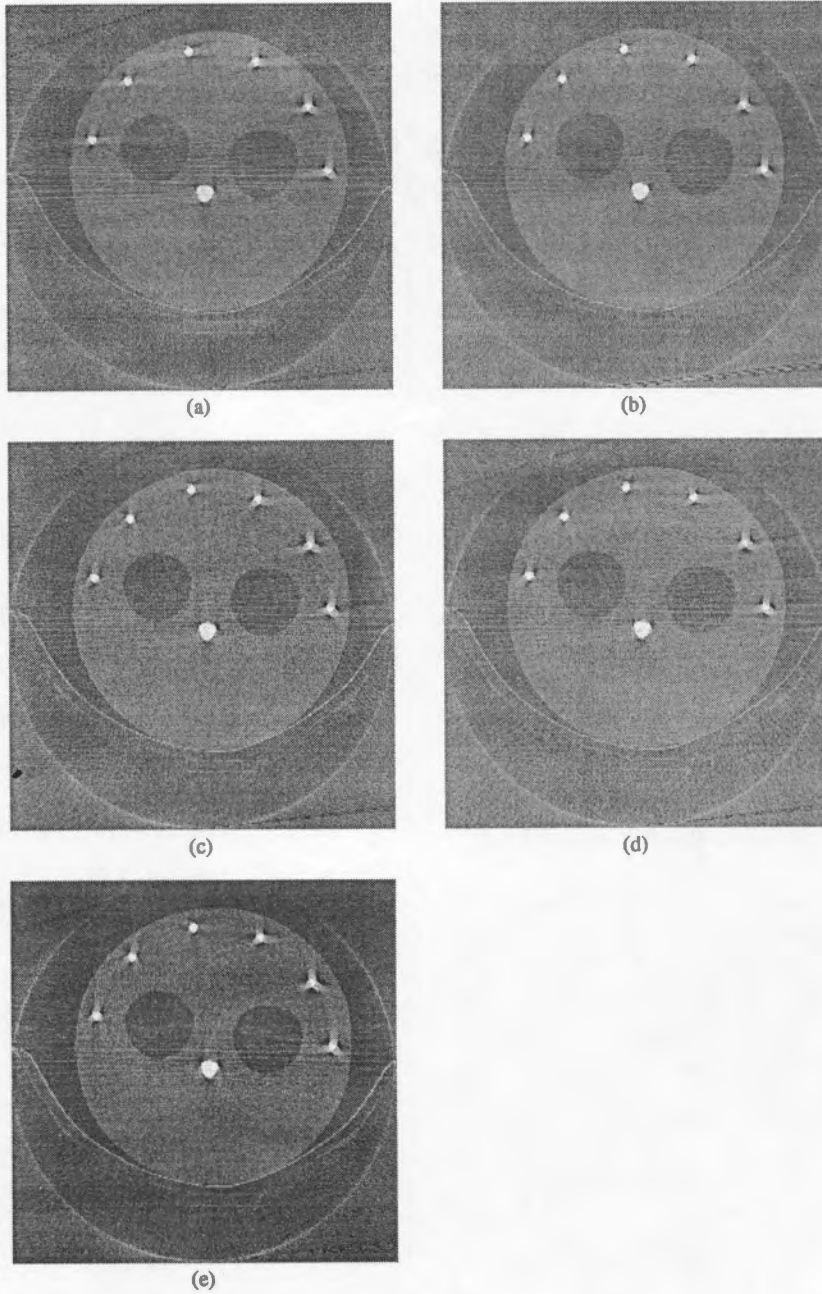


Figure 4.1: A comparison of short-scan compensation techniques. (a) No compensation (b) Parker technique (c) Wang technique (d) Symmetric weighting (e) Missing data creation over 2π radians

discussed in the previous chapter. All the images in the figure are of the center slice ($z = 0$) of the phantom object. The additional sampling region Δ required for the Wang technique was created the same way as for the full 2π reconstruction (e). Missing projections up to the desired angle were constructed from the existing data using the symmetry of the system. For (c), a Δ of 0.35 radians was used, which is just under two full cone-angles.

No compensation for the short-scan was used for Fig. 4.1(a). Note the dark and bright "streaking" artifacts radiating from the aluminum pins, particularly the thick streaks in the horizontal directions¹. These artifacts are greatly reduced in (b) by the Parker pre-weighting function. The Wang (c) and symmetric weighting (d) techniques provide similar results and an improvement in image quality over (a), but do not appear to be as effective as the Parker technique. The best image is obtained by creating the missing projections using the symmetry of the system and then reconstructing over the full circle (e). In this last image, the directional streaking is all but eliminated and there is better contrast between the drilled holes, the Lucite, and the aluminum which results in sharper object boundaries. A comparison of (b) and (e) shows that the backprojection weighting imbalance (Fig. 3.5) in (b) is not readily apparent in the filtered images except as a loss of contrast, which may not be important for most applications.

Reconstruction times for (a-b, d) varied from each other by less than 6 percent. Image (c) took over 50 percent longer than (a), the shortest reconstruction, due mostly

¹Note that some radial streaking is normal around objects of such relative high density as the aluminum pins

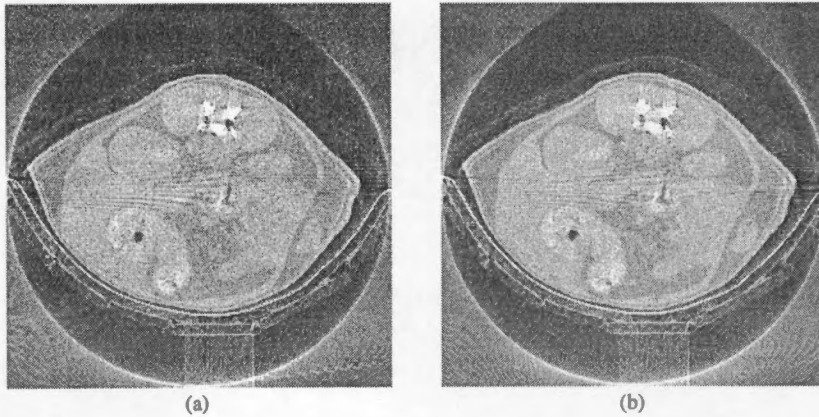


Figure 4.2: Comparison of mouse reconstruction using (a) Parker weighting and (b) missing data recreation technique.

to the enormous overhead of generating the data for the Δ range. If the extra data was available from the scan and did not need to be generated, the Wang technique could be expected to slow the process down over the Parker technique only as a linear function of the size of Δ , since both perform a preweighting step of similar computational complexity. The longest reconstruction by far was image (e), which took over five times as long to generate as (a) again due to the overhead required to fake missing data.

Fig. 4.2 is a comparison of slice $z = 0$ of a short-scan mouse reconstruction using the Parker pre-weighting function (a) and a full 2π reconstruction (b) using the technique of Fig. 4.1(e). The Shepp-Logan Fourier filtering technique was used for in both reconstructions. It is apparent that image (b) is less grainy and resolves more internal organ details. The cost of obtaining image (b), however, is again prohibitive, this time at almost nine times the reconstruction time of image (a). The increased disparity in reconstruction times from those for Fig. 4.1 is a result of the higher resolution of the

mouse scan, which requires a larger number of missing projections be created.

Because of the excessive processing time it requires, generating a theoretically correct image as in Fig. 4.1(e) and Fig. 4.2(b) is not practical unless the implementation is made much more efficient by parallelization or some other means. The best choice given the above results is probably to use the Parker technique, which gives fairly good images in a reasonable time frame.

Filtering techniques are contrasted in Fig. 4.3. The images are from the mouse data set and are the slice $z = -7$ of the reconstruction volume, an arbitrary location close to the midplane. Histogram specification was used to spread the graylevels so that internal details are more visible. The Parker short-scan weighting function was applied to projections prior to reconstruction.

No filtering was performed on projections prior to reconstruction in the first image (a), which illustrates the $1/|\vec{r}|$ blurring that occurs by backprojecting the Radon transform of an image. Only the outline of mouse is apparent in image (a), and no internal details can be seen. In (b), convolution filtering with a convolution kernel (Eqn. 3.8) truncated to size $k = 101$ was performed. The haze covering the image is a result of underfiltering and obscures many of the finer details. Fig. 4.3(c) shows how a much larger kernel $k = 501$ removes most of the haziness to produce a better image.

Filtering in (d-e) was done in the frequency domain and so makes use of the full filter width ($k = 1024$)². A ramp filter as described by Eqn. 3.13 was used to create

²Note that Fig. 4.2(a) and Fig. 4.3(e) are equivalent. The difference in their apparent contrast is due to the histogram specification performed on Fig. 4.3(e).

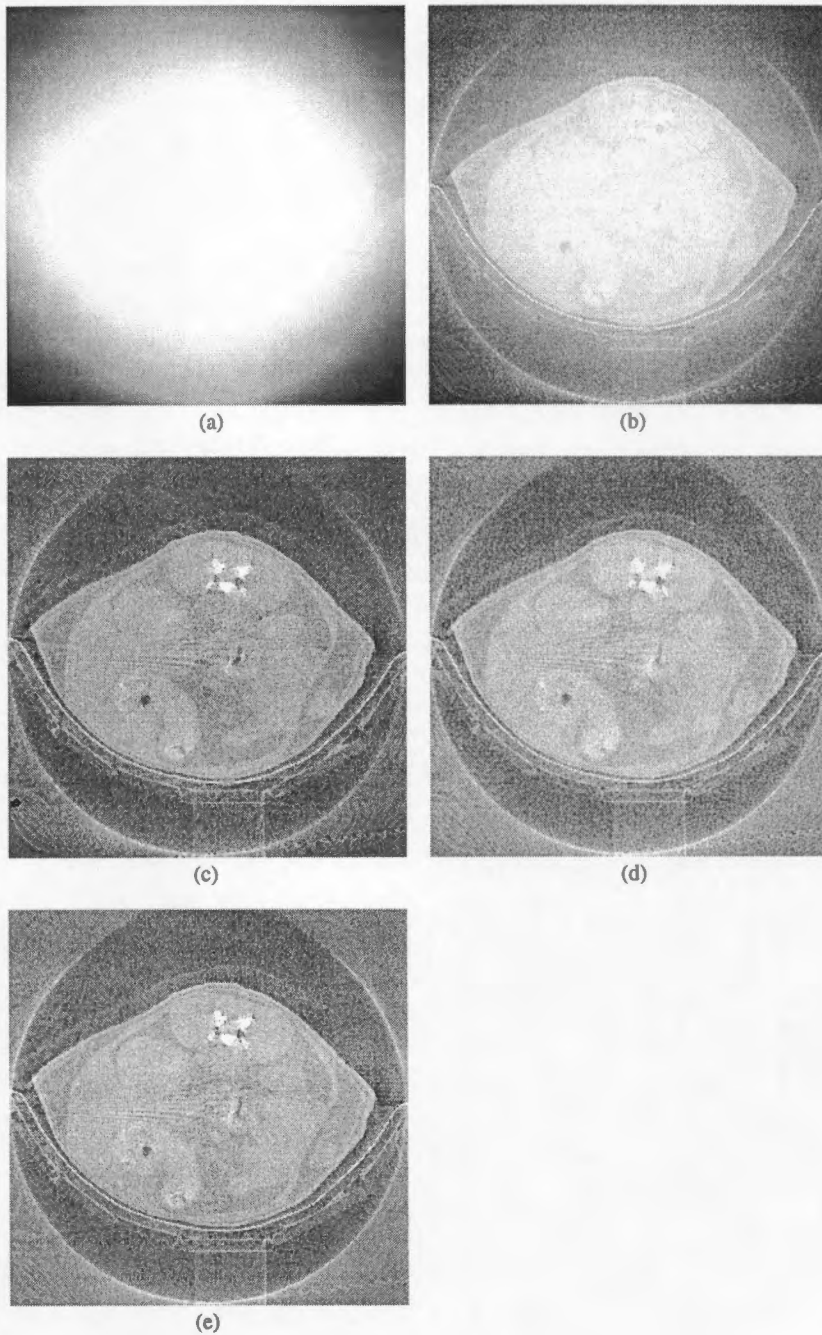


Figure 4.3: Comparison of filtering techniques. (a) Unfiltered (b) Small convolution kernel, $k = 101$ (c) Large convolution kernel, $k = 501$ (d) FFT filtering (full kernel) using ramp filter (e) FFT filtering using Shepp-Logan filter.

image (d) and the Shepp-Logan window (Eqn 3.14) was used for image (e). Image (d) is a noisier image than (e), which is to be expected since the Shepp-Logan filter is designed to suppress high frequencies associated with noise and is equivalent to the ramp filter with a smoothing window applied. The ramp filtered image has a grainier appearance and less detail is visible. Both images compare favorably to (c), with (d) showing slightly less detail and (e) slightly more.

Reconstruction times were comparable (within 3 percent) for the convolution filtered image (b) and the two fast Fourier transform filtered images. By contrast, the larger convolution kernel used in (c) increased the reconstruction time by almost 400 percent. Intermediately sized kernels produce a trade-off between speed and quality, and very small kernels $k < 100$ would save processing time if only the grossest of detail is required. But it is clear that for most MicroCAT applications, Fourier filtering using a Shepp-Logan window is the best of these options for both quality and speed of reconstruction.

Fig. 4.4 compares the effects of downsampling and bi-linear interpolation on image quality. All the images are of slice $z = -27$ of a reconstruction from $-127 < z \leq 0$ using the mouse data set. The reconstructions were done using Fourier filtering with the Shepp-Logan window and projections were pre-weighted using the Parker weight function.

The first two images (a-b) were constructed without downsampling the data. In (a), the truncation method of interpolation was used. This image is somewhat grainier in appearance than (b), which was created using bi-linear interpolation, supporting the

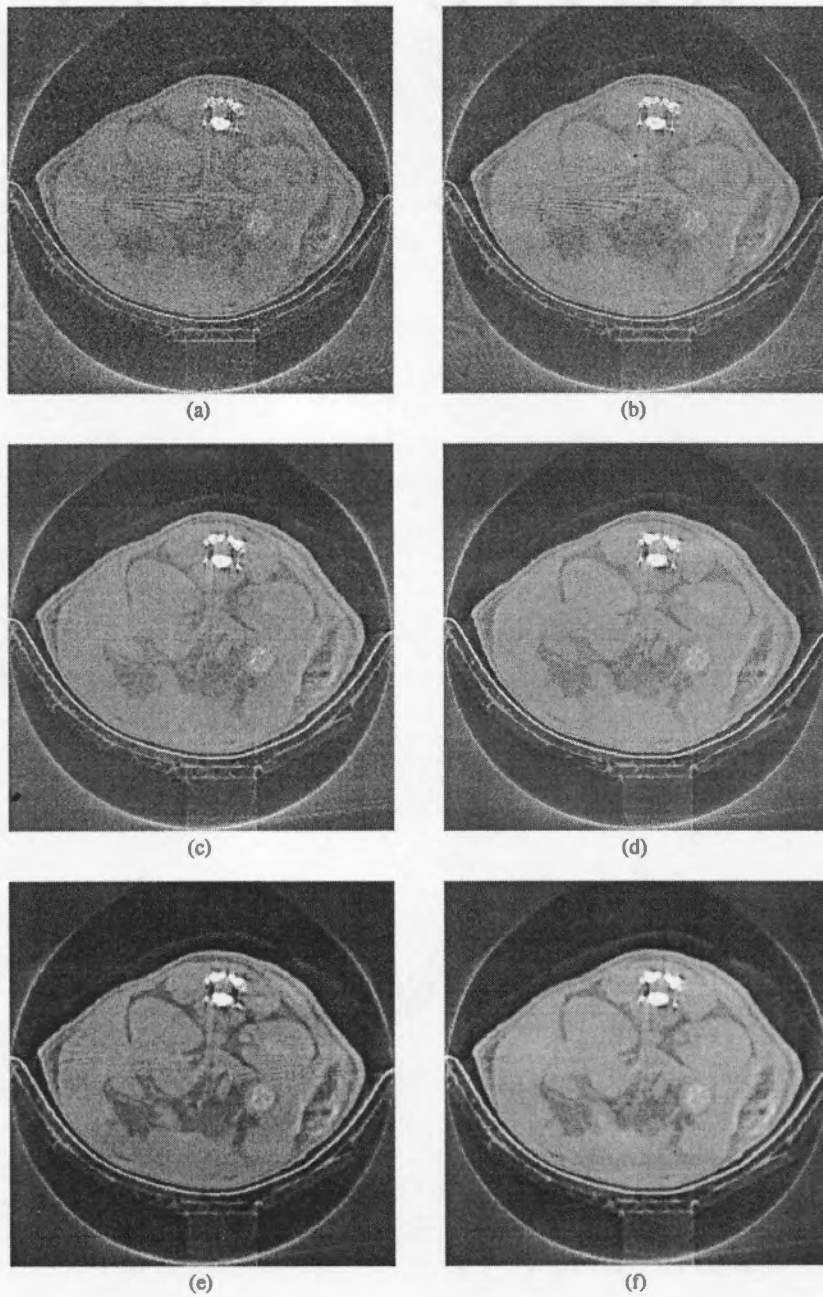


Figure 4.4: Comparison of the effects of downsampling and bi-linear interpolation on image quality. (a) Scale $t = 0$, truncation (b) $t = 0$, bi-linear interpolation (c) $t = 1$, truncation (d) $t = 1$, bi-linear interpolation (e) $t = 2$, truncation (f) $t = 2$, bi-linear interpolation.

Table 4.1 Reconstruction times from Fig 4 4 rounded to nearest minute. Backprojection was over the range $-127 < z \leq 0$, half of the volume depth.

Reconstruction	Total (min)	Backprojection	Filtering	Other
(a) $t = 0$ truncation	134	71	51	12
(b) $t = 0$ bi-linear	196	133	51	12
(c) $t = 1$ truncation	112	70	13	29
(d) $t = 1$ bi-linear	163	121	13	29
(e) $t = 2$ truncation	101	68	4	29
(f) $t = 2$ bi-linear	150	117	5	29

theory that the averaging effects of the bi-linear interpolation act to suppress noise and smooth the image. A dramatic increase in image quality is obtained when the projection data is downsampled by a factor of two (c-d), by setting $t = 1$ in Eqn 3 15. The improvement gained by using bi-linear interpolation (d) over truncation (c) is less noticeable in this downsampled set of images because of the Gaussian blurring and detector summing that have already taken place before backprojection

As the data resolution approaches that of the reconstruction, the reconstructed images start to blur. Images (e-f) were obtained by downsampling the data by a factor of four ($t = 2$) to produce 256×256 pixel projections, the same resolution as the reconstruction. This last set of images loses some of the finer details of the internal organs that can be seen in (c-d) Again, there is little discernible difference between bi-linear interpolation (f) and interpolation by truncation (e)

Table 4 shows reconstruction times for the volumes in Fig 4 4 Times are rounded to the nearest minute A substantial increase in backprojection times when using bi-

linear interpolation is apparent, almost 90 percent for the case $t = 0^3$. The overhead processing penalty for downsampling the image shows up as an increase in the “other” category for reconstructions (c-f). Note that this fixed cost buys a non-linear speedup in the filtering step as t is increased. We can also see from this table that the best quality images do not require the most processing time.

Fig 4.5 shows the axial distortion differences between the two algorithms using the mouse data set. The rebinned parallel reconstruction images are on the left (a,c,e) and the Feldkamp images are on the right (b,d,f). The Feldkamp reconstruction was done using Shepp-Logan Fourier filtering and Parker short-scan weighting. The center slices (a,b) compare favorably in quality, with (a) being slightly grainier in appearance and with some additional streaking around the spinal column near the top of the image, probably due to the use of the more noise-sensitive ramp filter. Moving outward from the midplane, the rebinned parallel reconstruction is beginning to develop artifacts around the bones of the spine (c) that are not evident in the Feldkamp reconstruction (d). Towards the edge of the reconstruction, these artifacts become much worse (e). By comparison, the Feldkamp algorithm (f) is showing some smearing of the bones of the now-visible ribcage (ring of bright points) and spine, but not nearly to the extent seen in (e).

Fig. 4.6 shows the z coordinates of the reconstruction slices in Fig 4.5 and the relative divergence of the fan-beams that were used to construct the slice. Note that

³The Feldkamp code implemented for the MicroCAT system is not necessarily optimized. It is possible, for example, that the disparity in backprojection times between bi-linear and truncation interpolations could be reduced.

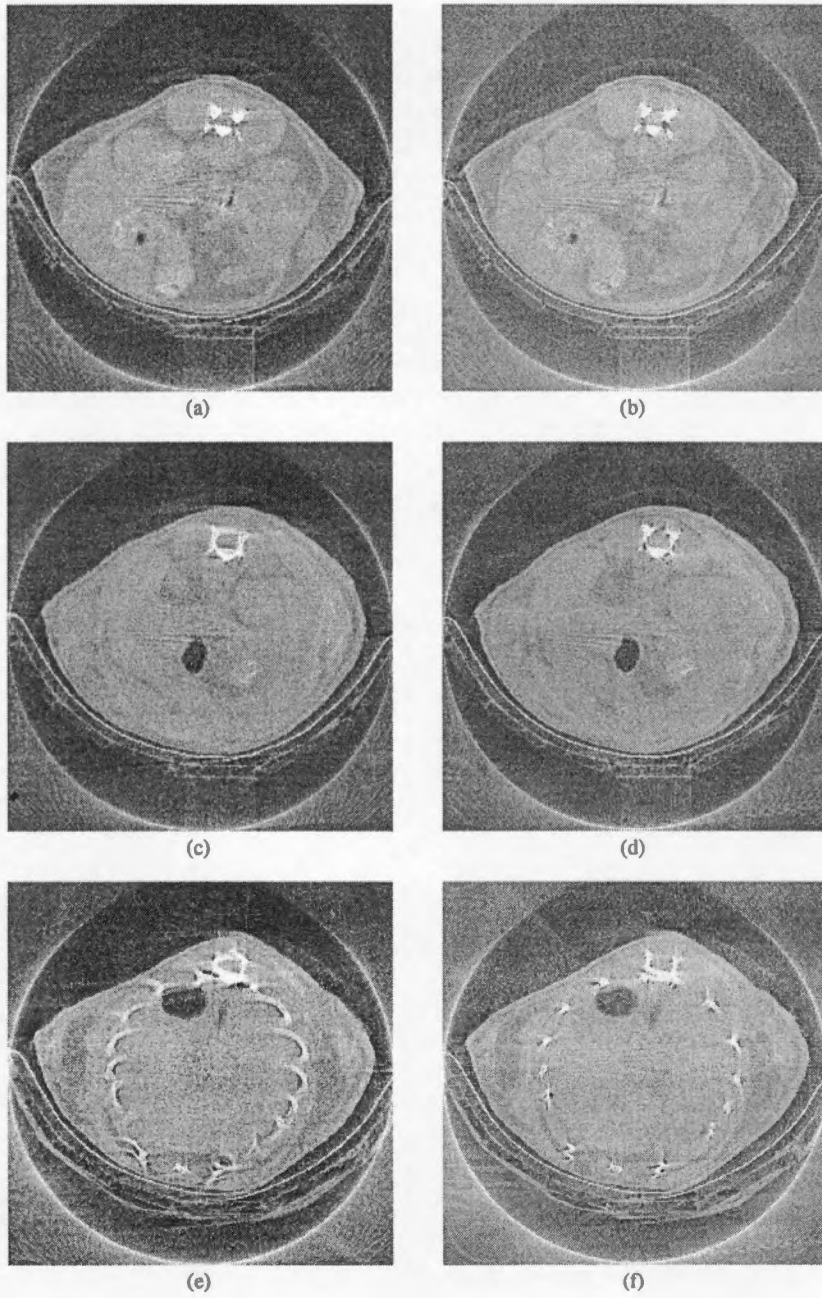


Figure 4.5: Axial distortion comparison of the fan-beam algorithm with the Feldkamp algorithm. Images are constructed from the mouse data set over $-127 < z \leq 0$. (a) $z = 0$ rebinned parallel (b) $z = 0$ Feldkamp (c) $z = -47$ rebinned parallel (d) $z = -47$ Feldkamp (e) $z = -107$ rebinned parallel (f) $z = -107$ Feldkamp

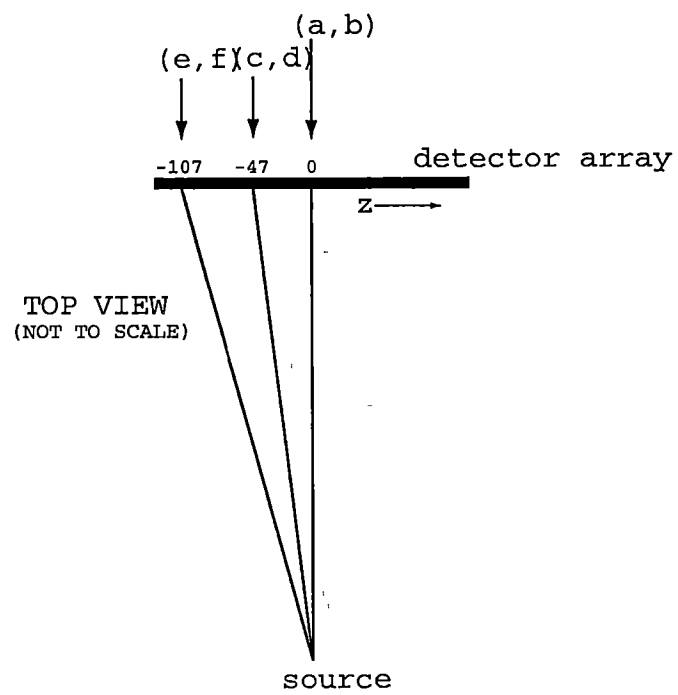


Figure 4.6: Relative distances along detector array of slices shown in Fig. 4.5.

this figure is not to scale, the cone-angle shown is much larger than the actual cone-angle

It is difficult to make a fair comparison of Feldkamp reconstruction times with those of the current method. What constitute comparable reconstruction volumes between the two algorithms is not clear. The rebinned fan-beam method creates a volume as a stack of individually reconstructed slices and without further study, it is not known what resolution in terms of number of these slices is required to emulate a Feldkamp volume of a particular z resolution. Such a judgement would be largely subjective anyway. The only meaningful comparison of times would be to establish criteria as to what constitutes a quality reconstruction from researchers who conduct mouse screenings with the MicroCAT system, and then determine the minimal times to create appropriate reconstructions using both methods.

Lacking such criteria, we will compare times for images judged to be of comparable quality (disregarding axial distortion differences) such as those in Fig. 4.5. Both the rebinned parallel-beam images and the Feldkamp images were obtained using a linear interpolation during the backprojection, and a Fourier based filtering method. No optimizing short-cuts were used in either reconstruction.

A complete $256 \times 256 \times 256$ reconstruction using the Feldkamp method, with all parameters as in Fig. 4.5, requires a total processing time of about 200 minutes. This averages to about 47 seconds per slice, where a "slice" is the plane of the object at each increment of z perpendicular to the axis of rotation, as depicted in the figures above. A "slice" from the rebinned parallel-beam reconstruction method is defined as a similarly

oriented image plane, but having a width corresponding to a single detector on the detector array. Thus a full reconstruction for comparison purpose consists of 1024, 256×256 slices, takes around 180 minutes at about 11 seconds per slice. It is not clear what percentage of the total slices are needed to create a volume that does not suffer in axial-spatial resolution, so it is not possible to say whether a full reconstruction with the current method is faster or slower than the Feldkamp method.

It is possible to compare the times required for the single images as seen in the above figures. Regardless of their “thickness”, the slices depicted show a similar resolution and quality. The current method of reconstruction is about four times as fast when analyzed on a per-slice basis. Its greatest speed advantage is that because it is a two-dimensional reconstruction method, slices can be fully constructed one-at-a-time, whereas the three-dimensional Feldkamp algorithm requires the full volume be constructed before any slices can be extracted. Note that reconstruction with the current method of a slice through the object not perpendicular to the z axis also requires a full volume reconstruction.

The per-slice times of the Feldkamp volumes can be reduced using the techniques explored in Fig. 4.4. From Table 4.1, we might expect a 46 percent decrease in backprojection time by eliminating bi-linear interpolation and a 74 percent decrease in filtering times by downsampling the projection data to half its resolution. Adding in the fixed overhead required for downsampling, these optimizations would decrease the per-slice reconstruction time to around 28 seconds (and provide better images in the process).

This chapter has provided evidence that the Feldkamp algorithm is a useful tool for

the MicroCAT, providing images of higher quality at an acceptable cost in reconstruction time. The various techniques of short-scan compensation, downsampling, and bi-linear interpolation were compared and the best options among them analyzed. In particular, it was shown that by downsampling and pre-weighting the projection data with the Parker weight function, higher quality images can be obtained in shorter times than by using the data at full resolution. The Fourier filtering technique proved to be a more efficient filtering method than convolution filtering. And bi-linear interpolation was shown to come at a high cost in backprojection time, while giving only marginal improvement in image quality when applied to downsampled data.

Chapter 5

Conclusions

This chapter presents some conclusions about the work completed for this thesis project, and suggests future work to address unresolved issues. It is organized as follows. The main problem addressed and the hypothesized solution are first revisited. Some issues that came about in implementing that solution are next discussed, followed by a review of its demonstrated effectiveness. The chapter concludes by suggesting a body of future work to resolve pending questions and to build on the groundwork already in place.

The MicroCAT tomography system under development for the Mammalian Genetics Research Facility at ORNL suffers from an inadequate method of image reconstruction. The current method utilizes two-dimensional reconstruction techniques on three-dimensionally acquired data, treating diverging fan-beams as a set of parallel fan-beams whose reconstructed image planes are stacked to form a volume. The result is an image volume that is only correct near the central plane ($z = 0$) of the image, where the

approximated geometry matches the true geometry, and becoming highly distorted at more distal axial locations

Because of the problems with the current reconstruction method, a new method that can perform a true three-dimensional volume reconstruction is desired for the MicroCAT system. Reconstruction speed is a high priority given its intended purpose of mass screenings of mice for phenotypic abnormalities, so, ideally, the volumetric algorithm chosen should be able to provide images in times comparable to those currently achieved. Another factor in the selection of a new algorithm is the hardware constraint that currently limits scans to a circular source trajectory

The Feldkamp cone-beam tomographic reconstruction algorithm for circular source trajectories was chosen as a possible solution to the problem for several reasons. It is widely recognized to be among the most computationally efficient of the filtered backprojection algorithms, which, in turn, are the most efficient of the cone-beam tomography algorithms in general. Other reasons to choose Feldkamp is that it is easily extended to accommodate other scanning geometries and is highly suited for parallelization.

A disadvantage of the Feldkamp algorithm, is that it is an approximate algorithm, based on the assumption that the contribution to the reconstruction volume from divergent fan-beams can be calculated analogously to the contribution in the midplane. Additionally, it suffers from artifacts due to the circular source trajectory on which it is based. Such a trajectory violates the completeness condition for cone-beam tomography, which requires that every possible plane through the object intersect at least one

point on the scanning trajectory. Violating this condition produces an incomplete set of ray-sums, making an exact reconstruction impossible. But even with its approximate nature, it was judged that the Feldkamp algorithm would provide an improvement over the current method and produce the best speed/quality tradeoff over other cone-beam methods.

Implementation of the algorithm was hindered by the MicroCAT system's inability to scan a full 360 degree set of data. Several methods of compensating for the missing scan angles were explored based on the approximate symmetry of the data. None of these methods is completely effective because they all rely on an incorrect assumption of rotational symmetry and a minimally complete set of ray-sums that cannot be found because of the circular source trajectory of the system. The most effective compensation technique was to create the missing projections as symmetric mappings of existing ray-sums, and then reconstruct over the full circle. Unfortunately this method is much too slow to be practical. It was shown that the Parker method, in which projections are preweighted to factor out redundant ray-sums in the minimally complete data set, gave only slightly less attractive results without any significant loss in speed.

A dramatic decrease in the time required to filter the images was achieved by downsampling the projection data prior to processing. Downsampling also produced much clearer images by averaging out the effects of noise while effectively increasing detector counts. Only when the downsampled data approaches the resolution of the projection data does the resulting image begin to lose resolution.

The Feldkamp implementation also explored the issue of the best method of interpolation among detector positions during backprojection. Truncating the floating point projected value to an integer detector position proved to be much faster than performing bi-linear interpolation. Bi-linear interpolation produced improved results, reducing noise and graininess of the image, but only slightly so in downsampled images where Gaussian blurring and detector summing have taken place. In fact, downsampling the data and using the truncation interpolation method was judged to give the best reconstruction speed / image quality tradeoff.

Comparing images created from a mouse data set using the Feldkamp implementation with those using the current rebinned parallel-beam reconstruction method, we found that, in the midplane, comparable results were obtained. But moving axially off of the midplane, the current method caused gross distortion of key anatomical features, while the Feldkamp images remained fairly accurate.

An analysis of reconstruction times showed that the Feldkamp algorithm is able to produce full volume reconstructions with a loss of only about ten percent in speed, although the average reconstruction time for a single "slice" of the volume is about four times longer. But it is not a straightforward matter to compare results from the two algorithms because they are not producing the same type of reconstruction. A volume created using stacked parallel-beam reconstructions is not necessarily comparable to a volume created using Feldkamp. More work would be required to understand the degree of accuracy actually needed in practice, and how efficient each method is in achieving

that accuracy.

In summary, a volumetric algorithm was successfully implemented for the MicroCAT system and is effective in overcoming the problem of axial distortion. Theoretically, even better results are obtainable with the algorithm if the MicroCAT can be reconfigured to allow a full 2π radian scan. As it stands, very good images are obtained using a set of techniques designed to overcome the lack of data and to sample the existing data to full effect. The Feldkamp algorithm is designed to reconstruct full volumes, and when used for this purpose does not present an increase in processing time over the current method.

The analysis given of the Feldkamp implementation and its comparison with the current method satisfies the question of its probable effectiveness for mouse screening studies, but it is neither rigorous nor complete. For example, only slices perpendicular to the z axis were compared, whereas the current stacking method may create other artifacts which are not seen from true, volumetric reconstructions. Note also that the best assessment of a reconstruction algorithm is a measurement of how accurately it reproduces the actual attenuation coefficients of the materials scanned, while the results given here are only subjective impressions of visual quality and do not necessarily have anything to do with reconstruction accuracy. Whether or not a more rigorous study of the implementation is warranted depends on the applications for which it is ultimately used.

Future work is warranted in order to optimize the algorithm for speed. We have

already seen that reconstruction quality is more sensitive to some steps in the Feldkamp algorithm than others. For example, the mis-weighting of the backprojected data when reconstructing from a short-scanned data set turned out not to be a significant problem as long as the effects of doubly sampled data were factored out. The method of interpolation became less critical when the projection data was smoothed and downsampled, saving considerable time during backprojection. There may be other processes in the algorithm that can be optimized for speed. A thorough analysis of the various tradeoffs between reconstruction times and image quality requires the input of those researchers who use the MicroCAT system. With their criteria as to what constitutes a "quality" image, the algorithm could be optimized to provide the fastest screening times yielding acceptable image quality.

Parallelization is the ultimate optimization for the Feldkamp algorithm and should prove to be a feasible solution in the context of the MicroCAT system. The assembly-line nature of the reconstruction process is ideal for implementation in a parallel environment, such as a local network of inexpensive workstations. A parallelized Feldkamp algorithm has already been shown by other researchers to be a very efficient means of near real-time tomographic reconstruction.

If the MicroCAT can be reconfigured to accommodate a full circular scan, a simultaneous rotation of the source around the object while translating the object in the z direction on its bed would produce a helical scan. A helical scan satisfies the completeness condition for cone-beam tomography and so provides the complete set of ray-sums

necessary for exact reconstruction. The Feldkamp algorithm is easily extended to a general form that will process helical data and provisions have already been made for that extension. Though an exact reconstruction would still not be possible, using helical data should eliminate any artifacts associated with the violation of the completeness condition.

More work is needed on the Feldkamp implementation to desensitize it to inevitable miscalibrations in the scanner hardware. Many scans suffer from a misalignment of the detector array with the center of the x-ray beam, which alters the geometry of the system by offsetting the true center of the detector array from the assumed center. The data sets used for experimental work on this project have a miscalibration of only a few hundredths of a percent, which does not appear to cause any significant disturbance in the reconstruction at the resolutions used. Other data sets have shown misalignments of over a tenth of a percent, which introduces considerable distortion of the reconstructed image. If the degree of misalignment can be determined, it is easy to correct for the offset problem in the backprojection by redefining the assumed center of the detector array to align with the actual center. Currently, however, the effects of misalignment on the weighting and rotational symmetry of projection data have not been examined. Filtering is independent of the cone-beam orientation, but short-scan compensations and the Feldkamp cosine and backprojection weights are based on an assumed symmetry of the cone-beam across the two axes of the projection, which is invalid when the beam is not perfectly aligned. More study is required to analyze the sensitivity of the algorithm.

to changes in beam symmetry, and how to algorithmically correct for it.

This thesis project has taken the first steps in realizing the MicroCAT's full potential as a true, third-generation scanner. The use of the Feldkamp algorithm for volumetric reconstructions has proven to be an efficient way to obtain higher quality images than the current method in use. Its main strength is in preserving structural integrity of the image towards the distal ends of the reconstruction volume. The implementation of the Feldkamp algorithm has a number of parameters that can be adjusted to improve the visual quality of the results and to shorten reconstruction times. Work is still needed to deal with the effects of scanner miscalibrations. Further comparisons of reconstruction quality between the current method and the Feldkamp method may also be warranted, but require the establishment of working criteria to define "quality" in a reconstruction. Additional work to parallelize the Feldkamp implementation and convert to a helical scanning trajectory is recommended in order to optimize reconstruction times and minimize data-related artifacts.

BIBLIOGRAPHY

Bibliography

- [1] R. Clack Overview of reconstruction algorithms for exact cone-beam tomography. *Proceeding of the the International Society for Optical Engineers*, 2299:230–241, 1994
- [2] L.A. Feldkamp, L.C Davis, and J W Kress Practical cone-beam algorithm. *Journal of the Optical Society of America*, 1(6):612–619, 1984
- [3] S. S. Gleason, H Sari-Sarraf, M. J Paulus, D. K. Johnson, S. J. Norton, and M.A. Abidi Reconstruction of multi-energy x-ray computed tomography images of laboratory mice. *IEEE Transactions on Nuclear Science*, 46(4) 1081–1086, 1999.
- [4] G.T. Herman, A V. Lakshminarayanan, and A Naparstek Convolution reconstruction techniques for divergent beams *Computations in Biological Medicine*, 6:259–271, 1976
- [5] H. P Hiriyannaiah X-ray computed tomography for medical imaging *IEEE Signal Processing Magazine*, 14(2):42–59, 1997

- [6] A. K. Jain *Fundamentals of Digital Image Processing* Prentice Hall, Englewood Cliffs, NJ, 1989
- [7] C. Laurent, F. Peyrin, J.M. Chassery, and M. Amiel. Parallel image reconstruction on MIMD computers for three-dimensional cone beam tomography. *Parallel Computing*, 24:1461–1479, 1998
- [8] D. L. Parker. Optimal short scan convolution reconstruction for fanbeam CT. *Medical Physics*, 9(2) 254–257, 1982.
- [9] M.H. Paulus, H. Sari-Sarraf, S.S. Gleason, et al. A new x-ray computed tomography system for laboratory mouse imaging. *IEEE Transactions on Nuclear Science*, 46(3):558–654, 1999
- [10] P. Rizo, P. Grangeat, P. Sire, P. Lemasson, and P. Melennec. Comparison of two three-dimensional x-ray cone-beam-reconstruction algorithms with circular source trajectories. *Journal of the Optical Society of America*, 8(10).1639–1648, 1991.
- [11] A. Rosenfeld and A. C. Kak. *Digital Picture Processing* Academic Press, New York, NY, 1976
- [12] B. D. Smith. Cone-beam tomography: recent advances and a tutorial review. *Optical Engineering*, 29(5).524–534, 1990.
- [13] B. D. Smith and C. C. Peck III. Implementations, comparisons, and an investigation of heuristic techniques for cone-beam tomography. *IEEE Transactions on Medical Imaging*, 15(4):519–531, 1996

- [14] H. Tuy. An inversion formula for cone-beam reconstruction *SIAM Journal of Applied Math*, 43:546–552, 1983
- [15] G. Wang, T. Lin, and P. Cheng. Half-scan cone-beam x-ray microtomography formula. *Scanning*, 16 216–220, 1994.
- [16] G. Wang, T. Lin, P. Cheng, and D. M. Shinozaki. A general cone-beam reconstruction algorithm *IEEE Transactions on Medical Imaging*, 12(3):486–496, 1993.
- [17] H. Wechsler. *Computational Vision*. Academic Press, San Diego, CA, 1990

APPENDICES

Appendix A

In this appendix, we show the process of deriving Eqn. 2.6 from the inverse of the Radon transform. The Fourier transform is introduced into Eqn. 2.4, and the inner integral is evaluated. Principal value integration is used for the evaluation because of the singularity at $l = 0$.

From Eqn. 2.5,

$$\frac{\partial}{\partial l} g(l, \theta) = \frac{i\omega}{2\pi} \int_{-\infty}^{\infty} \exp(i\omega l) q(\omega, \theta) d\omega \quad (\text{A.1})$$

Substituting Eqn. A.1 into Eqn. 2.5 and changing the order of integration gives

$$f(r, \phi) = \frac{i}{8\pi^3} \int_0^{2\pi} \int_{-\infty}^{\infty} \omega q(\omega, \theta) \int_{-\infty}^{\infty} \frac{\exp(i\omega l)}{r \cos(\theta - \phi) - l} dl d\omega d\theta \quad (\text{A.2})$$

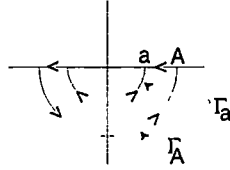
Isolating the inner integral, we perform the principal value integration as

$$\int_{-\infty}^{\infty} \frac{\exp(i\omega l)}{r \cos(\theta - \phi) - l} dl = \lim_{A \rightarrow \infty, a \rightarrow 0^+} \left(\int_{-A}^{-a} + \int_a^A \right) \frac{\exp(i\omega l)}{r \cos(\theta - \phi) - l} dl \quad (\text{A } 3)$$

Changing variables so that $c = r \cos(\theta - \phi) - l$ and $k = c - l$ gives us,

$$\begin{aligned} & \lim_{A \rightarrow \infty, a \rightarrow 0^+} \left(\int_{c+a}^{c+A} + \int_{c-A}^{c-a} \right) \frac{\exp(i\omega(c-k))}{k} dk \\ &= \exp(i\omega c) \lim_{A \rightarrow \infty, a \rightarrow 0^+} \left(\int_{c-A}^{c-a} + \int_{c+a}^{c+A} \right) \frac{\exp(-i\omega k)}{k} dk \end{aligned} \quad (\text{A } 4)$$

Suppose that $\omega > 0$. Consider $\int_{\Gamma_{a,A}} \frac{\exp(-i\omega z)}{z} dz$ where $\Gamma_{a,A}$ is given by,



such that,

$$0 = \left(\int_A^a + \int_{-a}^{-A} \right) \frac{\exp(-i\omega k)}{k} dk + \int_{2\pi}^{\pi} \exp(-i\omega a \exp(i\gamma)) d\gamma + \int_{\pi}^{2\pi} \exp(-i\omega A \exp(i\gamma)) d\gamma \quad (\text{A.5})$$

Note that

$$\lim_{a \rightarrow 0^+} \int_{2\pi}^{\pi} \exp(-i\omega a (\cos \gamma + i \sin \gamma)) i d\gamma = \int_{2\pi}^{\pi} i d\gamma = -i\pi \quad (\text{A.6})$$

and because $\sin \gamma > 0$ on $(\pi, 2\pi)$,

$$\left| \lim_{A \rightarrow \infty} \int_0^\pi \exp(-i\omega A(\cos \gamma + i \sin \gamma)) i d\gamma \right| \leq \lim_{A \rightarrow \infty} \int_0^\pi \exp(\omega A(\sin \gamma)) d\gamma = 0 \quad (\text{A.11})$$

From Eqns A.9–A.11 we conclude that

$$\int_{-\infty}^{\infty} \frac{\exp(-i\omega k)}{k} dk = i\pi, \quad \omega < 0 \quad (\text{A.12})$$

Substituting the results from Eqns. A.8 and A.12 into Eqns. A.4 and A.3 gives us the solution for the principle value integration,

$$\int_{-\infty}^{\infty} \frac{\exp(i\omega l)}{r \cos(\theta - \phi) - l} dl = \begin{cases} -i\pi \exp(i\omega r \cos(\theta - \phi)), & \omega > 0 \\ i\pi \exp(i\omega r \cos(\theta - \phi)), & \omega < 0 \end{cases} \quad (\text{A.13})$$

By substitution of this result into Eqn A.2 we arrive at Eqn 2.6

$$f(r, \phi) = \frac{1}{8\pi^2} \int_0^{2\pi} \pi \int_{-\infty}^{\infty} |\omega| q(\omega, \theta) \exp(i\omega r \cos(\theta - \phi)) d\omega d\theta$$

Vita

Joshua Edward Cates was born on May 24, 1972 in Los Alamos, NM. He attended grade schools there and in Oak Ridge, TN, culminating in a high school diploma from Oak Ridge High School in 1990. He spent the subsequent four years in scholarship and service to the microbiology, animal behavior, and electron microscopy laboratories of the University of Tennessee, Knoxville, where he was awarded a Bachelor of Science degree with highest honors in Organismal and Systems Biology with a minor in Mathematics in December 1994. A lingering fascination with complex systems and mathematical modeling prompted him to begin work towards a Master of Science Degree in Computer Science at the University of Tennessee, Knoxville in the summer of 1997. When not thinking about computation or other such scholarly matters, he likes to write music and get lost in the woods.